A wind turbine digital shadow for complex inflow conditions

Hadi Hoghooghi and Carlo L. Bottasso

Wind Energy Institute, Technical University of Munich, 85748 Garching b. München, Germany

Correspondence: Carlo L. Bottasso (carlo.bottasso@tum.de)

Abstract.

We present a digital shadow Kalman filtering ~~approach~~ framework based on the direct linearization of a ~~multibody aeroservoelastic model of a wind turbine~~ trusted multibody aeroservoelastic wind turbine model. In contrast to ~~approaches~~ shadowing based on ad hoc ~~models, the reuse of existing trusted~~ modeling approaches, reusing validated industrial or research-grade models reduces development ~~time and duplication of~~ effort, leverages resources invested in tuning and validation, and eventually increases confidence in the results.

~~This approach has already been pursuded by others, but it is here improved with respect to several main aspects of the formulation. To extend the applicability to~~ Building on earlier work, the filter-internal model is extended to improve applicability under non-symmetric, waked, and yaw-misaligned ~~conditions, the filter-internal model – in addition to the~~ inflow conditions. In addition to tower fore-aft and ~~rotor rotational dynamics – now also includes the~~ rotor-speed dynamics, the model incorporates tower side-side ~~and the~~ motion as well as blade flapwise and edgewise degrees of freedom~~of the rotor blades. To make the model aware of the inflow conditions at the rotor disk, inflow estimators are used to detect in real time during operation~~ . Real-time inflow observers estimate rotor-equivalent ~~values of the~~ wind speed, vertical ~~shear, horizontal shear(on account of waked conditions)~~and horizontal shear, and yaw misalignment~~(in support of wake-steering control). These inflow parameters are used to schedule the filter-internal model, adapting its behavior to the current conditions experienced by the turbine. Furthermore, the filter-internal~~ , enabling operating-point-dependent scheduling of the linearized model. To further enhance predictive accuracy, the white-box model is augmented with data-driven corrections~~to improve its predictive accuracy. Two approaches are explored for the correction of the model: a bias correction method that attempts to improve both~~ , considering both a bias-correction approach that acts on states and outputs, and a ~~neural-based one that only corrects the outputs but not the states~~neural-network-based output correction.

The proposed ~~digital shadow is demonstrated first in a simulation environment, considering clean~~ method is validated in simulation under freestream, waked, and wake-steering ~~conditions, and then using a field dataset collected on an instrumented turbine. To further validate its performance under complex inflow conditions, additional field data evaluations are conducted, including cases of extreme vertical shear , waked, and wake-steering conditions. Remarkably, the quality of the estimates of the damage equivalent loads for the field case is similar to the simulation case, even without any specific correction of the filter-internal model. However, after applying correction techniques, the quality of the estimates improves drastically, yielding errors in the damage equivalent load estimates of~~ scenarios and subsequently on field data from an instrumented wind turbine. Additional field cases with extreme shear and waked operation are used to assess robustness. Even without data-driven

correction, damage-equivalent loads estimated from field data exhibit accuracy comparable to simulation-based results. When correction strategies are applied, accuracy improves substantially, with damage-equivalent load errors reduced to only a few ~~percentage points.~~

percent.

1 Introduction

Digital twins for wind turbine applications have recently ~~received a significant attentionfrom the research community, on their way to become~~ garnered significant attention, emerging as key components of modern wind systems. ~~Digital twins can play various roles in multiple applications, including the support of control systems (Anand and Bottasso, 2023), the estimation of consumed and remaining lifetime~~ They support control (Anand and Bottasso, 2023), lifetime estimation (Branlard et al., 2020b; Song et al., 2023), and ~~the monitoring of the condition of assets (Olatunji et al., 2021). In fact,~~ asset monitoring (Olatunji et al., 2021). Because wind turbines operate autonomously in complex ~~, dynamic, and often harsh ambient conditions. The~~ and variable conditions, the ability to mirror the behavior of each asset ~~with its own digital replica clearly has a very significant potentialand a wide scope. Additionally, by combining data~~ offers substantial potential. Combined with machine learning and artificial intelligence, ~~the quality of the digital copy can be improved over time, with obvious benefits in~~ digital representations can continually improve, thereby enhancing productivity and profitability.

Digital twins ~~provide services by building~~ build on the predictive abilities of digital shadows~~. In fact, a digital shadow is a mirror of an asset obtained through a~~ , which rely on a one-way data flow ~~(from~~ from the physical asset to ~~digital model), whereas a digital twin is based on a two-way data flow that closes the loop between the virtual and physical entities (Sepasgozar, 2021). This paper focuses on the formulation of a method to mirror the behavior of an asset, while the loop closure is not specifically considered here. Therefore, the term digital shadow, instead of digital twin, is preferred in the present context~~ the model, unlike twins, where the loop is closed (Sepasgozar, 2021). As this work focuses solely on accurate mirroring, we adopt the term *digital shadow* (Hoghooghi et al., 2024).

~~There is clearly a plethora of ways to develop digital shadows. Here, we expand on an approach based on the integration of~~ Among the many possible formulations, we follow and extend an approach that integrates an aeroservoelastic model ~~of the machine~~ with a Kalman filter (Grewal and Andrews, 2014; Branlard, 2019; Branlard et al., 2024a; Hoghooghi et al., 2024). ~~Although this may seem to be a relatively standard and straightforward way of developing a digital shadow, it has a number of interesting characteristics. First, each wind turbine developer has trusted aeroservoelastic models of its turbines~~Wind turbine manufacturers already maintain trusted and validated aeroservoelastic models, which are ~~fine-tuned during design and often carefully validated with data from instrumented prototypes and field trials. These models seem to be ideally suited for developing digital shadowsinstead of creating new ad hoc models from scratch for this specific task. Second, developing a digital shadow from an existing model immediately gives a baseline predictive ability, even in the absence of~~ ideal candidates for the development of digital shadows. Using these models eliminates the need to rebuild ad hoc representations and provides immediate predictive capabilities, even without extensive field datasets ~~. On the other hand, –~~an advantage over purely data-

driven ~~black-box approachescan only be aware of the informational content of the data they are trained on. Long measurement times may be needed for collecting datasets that cover all the operating conditions of interest (including the ones at the boundaries of the operational envelope) and that possess sufficient statistical significance, in turn hindering the applicability of methods that exclusively rely on data. From this point of view, an approach based on an existing trusted aeroservoelastic model seems to be more appealing, especially when considering that such a white~~ approaches, which require lengthy and expensive measurement campaigns. Moreover, a white-box model can later be ~~turned~~ augmented with data-driven corrections, evolving into an adaptive grey model~~when augmented with corrective elements based on data~~.

~~The approach proposed here is based on the work of Branlard (2019) and Branlard et al. (2024a): an existing~~ Following Branlard (2019); Branlard et al. (2024a), an aeroservoelastic model is linearized around ~~a number of operating conditionsto define~~ multiple operating conditions, yielding a linear state-space ~~filter-internal model ;~~ internal model updated at each time step ~~, a Kalman filter is used to innovate the predictions of the model by using supervisory control and data acquisition (SCADA) measurementsfrom the operating asset, delivering estimates of the model states and of additional outputs of interest.~~

~~This existing approach is improved here~~ via SCADA measurements. Here, we improve this framework in four main ways.

First, ~~in addition to the~~ the internal model is expanded beyond tower fore-aft and ~~rotor rotational dynamics (Branlard, 2019; Branlard et al , the filter-internal model now includes also the~~ rotor-speed dynamics to include tower side-side ~~and the~~ motion and blade flap-wise and edgewise ~~degrees of freedom (DOFs) of the rotor blades~~DOFs. This richer ~~description of the system response is meant to enable the application of the digital shadow to more general operating conditions, as for example the ones in strongly shearedflows, or in wake overlap, or in yaw misalignment for~~ representation extends applicability to strongly sheared, waked, and yaw-misaligned conditions relevant to wake-steering ~~wind farm~~ control.

Second, ~~because of the wider range of possible operating conditions now supported by the digital shadow, a more sophisticated schedulingof its linear state-space filter-internal model is necessary. To this aim~~the wider operating envelope requires more advanced scheduling. Accordingly, the model is scheduled ~~here not only in terms of wind speed – as commonly done –, but also with respect to~~ not only by wind speed but also by vertical shear, horizontal shear (~~on account of possible~~ capturing wake impingement), and yaw misalignment. These ~~three extra scheduling parameters are tasked with informing the model of the current inflow conditions present at the rotor disk. These quantities are detected~~ inflow parameters are estimated in real time ~~during operation by dedicated observers (Kim et al., 2023; ?)~~using dedicated observers (Kim et al., 2023; Bertelè et al., 2024).

Third, a bias-correction ~~approach is used to improve~~ procedure improves the accuracy of ~~the filter-internal model. The approach is designed to compensate for possible biases in the estimation of both the system states and of the~~ both state and output equations. ~~To correct the system states, an error term is added to the dynamic force-balance equilibriumequations, and it is calibrated depending on the operating conditions. A more general approach would be to correct the stateequations with a non-linear error term, following for example Bottasso et al. (2006). This is a planned future improvement, and in fact the implemented Kalman filter is already able to handle non-linear models (Wan and Van Der Merwe, 2000), but this capability is not discussed further here. To correct the output equations, measurement~~ State biases are compensated through additive error terms in the dynamic equilibrium, calibrated as a function of the current operating state. Output biases are promoted to state variables ~~, whose dynamics are triggered by a dedicated process noiseterm. The approach is shown to yield a~~

~~considerable improvement in the quality of the estimationof fatigue damage~~governed by process noise. Although more general nonlinear corrections (Bottasso et al., 2006) are possible, the adopted approach already delivers substantial improvements in fatigue-damage estimation.

Fourth, for condition monitoring applications the model is ~~augmented by~~ enhanced via a data-driven learning element ~~to improve its predictive ability for condition monitoring (CM) applications. In such a case, the correction is only applied to specific outputs of interest for which measurements are available~~that corrects selected outputs using measurements from onboard sensors. A neural-based ~~correction term is~~ term is trained on the observed discrepancies and added to the ~~relevant model equationsand trained based on the measurements provided by on-board sensors. After learning, the model achieves a very high accuracy in the predictions of these outputs, which a CM system (not described here) can leverage by comparing predictions with measurements in order to detect possible anomalies and faults~~corresponding model equations, yielding highly accurate predictions suitable for anomaly detection.

The ~~proposed approach is first demonstrated in a simulation environment~~ digital shadow is demonstrated in simulation under clean freestream, waked, and wake-steering conditions~~and then validated in the field using~~ , and validated with field data from an instrumented multi-MW ~~wind turbine , encompassing~~ turbine under both clean and complex inflow~~conditions~~. The implementation ~~is based on the widely used open-source aeroservoelastic simulation environment OpenFAST and~~ utilizes OpenFAST and its associated tools (OpenFAST, 2024; Jonkman and Shaler, 2021; TurbSim, 2023), ~~while the filter is based on MATLAB (The MathWorks, Inc., 2022). Clearly,~~ with the filter realized in MATLAB (The MathWorks, Inc., 2022), although the methodology is ~~completely general and could be implemented in other software environments than the ones used here~~general and software-independent.

~~The literature on digital twins and their applications in wind energy is vast, especially on the topics revolving around structural fatigue~~ Fatigue-related applications of digital twins are extensively documented (Bernhammer et al., 2016; Hoghooghi et al., 2019a, b)~~. In fact,~~ , as fatigue loads affect ~~various wind turbine components – such as tower, blades, drivetrain, bearings, and others – causing permanent damage, in turn reducing lifetime, limiting revenue, and increasing operational costs (IEC, 2005; Hoghooghi, 2021). Consequently, fatigue reduction and lifetime estimation are areas of primary significance and interest for industry~~ all major components (IEC, 2005; Hoghooghi, 2021) and directly influence lifetime, performance, and cost (Bottasso et al., 2013; Loew and Bottasso, 2022; Dimitrov et al., 2018). ~~CM facilitates the real-time assessment of turbine health and performance, enabling proactive maintenance strategies to mitigate fatigue-induced failures and to optimize~~ Condition monitoring (CM) supports proactive maintenance and improved operational efficiency (Chen et al., 2016; Wu et al., 2021; Liu et al., 2023)~~. Therefore, accurate fatigue estimation, coupled with effective CM practices, is essential for enhancing performance and reducing costs~~ , with several methods leveraging machine learning (Bangalore et al., 2017; Hoghooghi et al., 2020a, b, 2021; Surucu et al., 2023).

~~The application of digital twin technology in condition monitoring and diagnosis offers numerous benefits. These include the optimization of fleet-wide performance, the continuous monitoring of critical components throughout their entire lifecycle, and the proactive planning of physical maintenance visits and repairs. Benefits also extend to other interesting applications, such as the training of maintenance engineers and technicians in virtual environments. All this has the potential for reduced costs, for~~

~~improved availability by minimizing downtime, and for a faster and more effective identification of inefficiencies. Additionally, digital twins enable the forecasting of failure modes and their likely consequences, providing unique insights into the health of mechanical components of wind turbines (Olatunji et al., 2021). Intelligent monitoring procedures, a primary responsibility of digital twins, can be implemented directly (offline) or indirectly (online). Offline monitoring involves periodic machine-assisted onsite inspections, necessitating operational interruptions. In contrast, online monitoring entails a continuous monitoring of equipment via sensors during operation (Chen et al., 2016; Bangalore et al., 2017; Wu et al., 2021; Surucu et al., 2023).~~

~~There is also an ample literature on methods for estimating fatigue loads. For example, hybrid techniques that combine physics-based methods with SCADA data have been demonstrated by Noppe et al. (2016). Various other load estimation techniques have been described and successfully employed, including~~ Numerous load-estimation techniques also exist, ranging from hybrid physics-data methods (Noppe et al., 2016) to lookup tables (Mendez Reyes et al., 2019), modal expansion (Iliopoulos et al., 2016), ~~ensemble aggregation of fatigue loads based on concurrent multiple simulations~~ ensemble-based fatigue aggregation (Abdallah et al., 2017), machine learning (Evans et al., 2018), neural networks ~~(NNs)~~ (Schröder et al., 2018), polynomial chaos ~~expansion~~ (Dimitrov et al., 2018), deconvolution (Jacquelin et al., 2003), load extrapolation (Ziegler et al., 2017), virtual sensing ~~based on reduced-order models (ROMs) extracted from finite element (FE) models~~ via ROM–FE coupling (Vettori et al., 2020), and NN-based ~~load~~ surrogates (Guilloré et al., 2024).

This ~~quick and necessarily incomplete overview of the vast literature on the subject gives an idea of the wide range of applications and benefits that digital twins may bring to the field. Yet, a successful digital twin must invariably rely on the modeling accuracy of its underlying digital shadow(s).~~ brief overview illustrates the broad relevance of digital shadows for turbine health monitoring and fatigue estimation. The present work contributes ~~to this important topic~~ by formulating a ~~procedure to develop digital shadows that leverage existing trusted multibody dynamics models, which often encapsulate a large body of experience and knowledge of wind turbine manufacturers. These models are linearized to increase computational efficiencyand then augmented with flow~~ general procedure for digital shadow development that leverages trusted multibody models, linearization for computational efficiency, and adaptive corrections informed by inflow estimators and learning elements ~~, yielding simple-to-use yet effective and adaptive mirroring capabilities of wind assets in their full range of operating conditions~~for improved accuracy.

The paper is organized as follows~~:~~ . Sect. 2 ~~outlines~~ describes the methodology, ~~detailing the filter-internal~~ including the internal model, its scheduling~~by inflow estimators, the correction of biases, and the a-posteriori data-driven adaptation of selected outputs. Section 3 characterizes the performance of the proposal digital shadow approach, first in a simulation environment considering clean freestream, waked, and wake-steering conditions, and then in the field using data from an instrumented multi-MW wind turbine, covering both clean and complex inflow conditions. Finally,~~ , and correction strategies. Sect. 3 evaluates performance in simulation and field conditions. Sect. 4 summarizes ~~the key~~ findings and outlines ~~the next steps in this research~~future work.

2 Methods

Figure 1 illustrates the ~~key~~ main components of the proposed digital shadow workflow. A Kalman filter ~~uses SCADA measurements to improve~~ combines SCADA measurements with the predictions of a turbine ROM ~~, in order to estimate the~~ to estimate system states and ~~other outputsof interest~~additional outputs. The filter-internal model is obtained by ~~linearization of~~ linearizing a higher-fidelity multibody model of the turbine. ~~Measurements of the blade loads are fused with the SCADA data stream to estimate some key characteristics of the inflow~~ Blade-load measurements are combined with SCADA data to infer key inflow characteristics in real time~~during operation. In turn, these~~ . These inflow parameters are ~~used for the scheduling of the~~ then used to schedule the coefficients of the filter-internal model, ~~thereby adjusting the filter behavior to~~ enabling the filter to adapt to the full range of operating and inflow conditions ~~to which the turbineis exposed to~~experienced by the turbine.

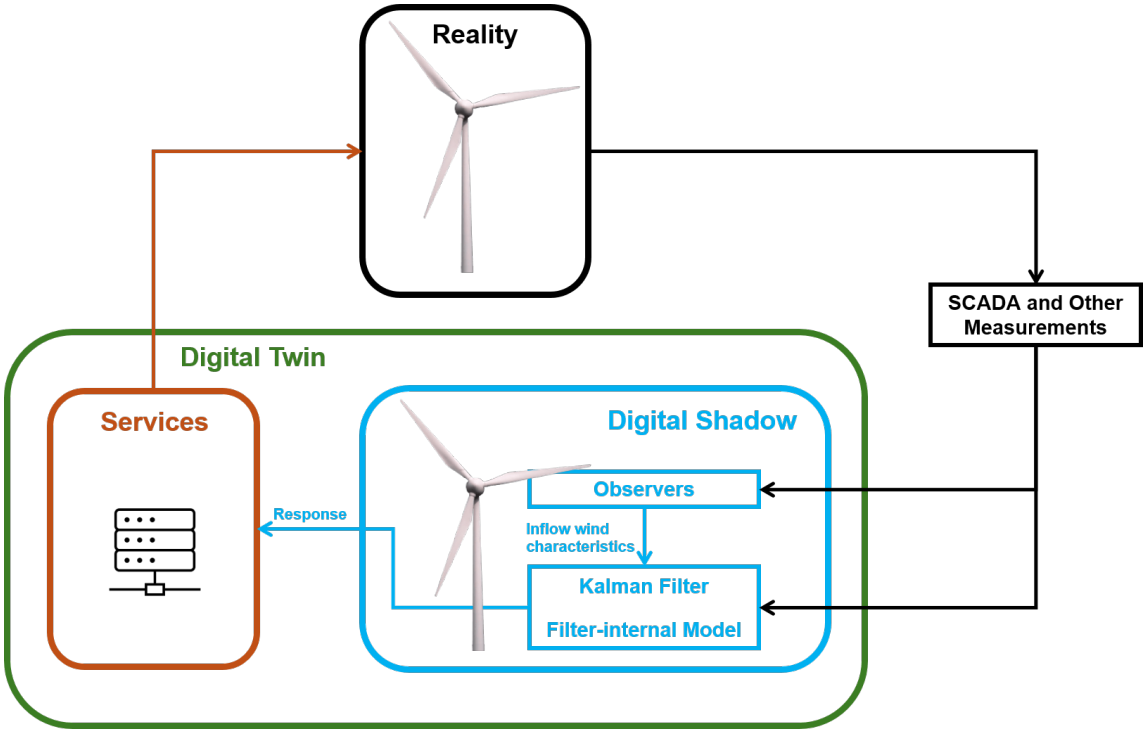

Figure 1. Schematic representation of the proposed digital shadowing approach.

The proposed digital shadow combines a physics-based reduced-order model with real-time measurements to continuously estimate the turbine dynamic state and selected unmeasured loads. The Kalman filter serves as the core data-fusion mechanism, propagating the turbine response using the linearized aeroelastic model and correcting these predictions whenever new measurements become available. Model scheduling ensures that the filter remains valid across varying inflow and operating conditions by adjusting the model coefficients in real time.

2.1 Filter-internal model

We consider a ~~non-linear~~ nonlinear multibody model of a wind turbine~~. The model is~~ , expressed in terms of ~~the~~ generalized displacements $\mathbf{q}$, ~~generalized~~ velocities $\mathbf{v}$, and inputs $\mathbf{u}$. ~~Measurements affected by noise ν are available for~~ Noisy measurements $\boldsymbol{\nu}$ affect the outputs $\mathbf{y}$ ~~, which are~~ used by the filter to ~~improve the prediction of the model states. Finally,~~ update the model states, while $\mathbf{z}$ ~~are additional output quantities~~ denotes additional outputs of interest that do not participate in the ~~filter~~ innovation step.

The filter ROM is obtained by directly linearizing the ~~non-linear multibody~~ nonlinear model around multiple equilibrium conditions~~where state, input, and output vectors are noted~~ , with equilibrium vectors $\mathbf{q}_0$, $\mathbf{v}_0$, $\mathbf{u}_0$, $\mathbf{y}_0$, and $\mathbf{z}_0$. The resulting filter-internal linear model is ~~written~~ formulated in terms of increments $\delta(\cdot)$ as

$$\dot{\delta\mathbf{q}} = \delta\mathbf{v}, \tag{1a}$$

$$\dot{\delta\mathbf{v}} = -\mathbf{M}^{-1}(\mathbf{C}\delta\mathbf{v} + \mathbf{K}\delta\mathbf{q} + \mathbf{U}\delta\mathbf{u} + \omega), \tag{1b}$$

$$\delta\mathbf{y} = \mathbf{D}_v\delta\mathbf{v} + \mathbf{D}_q\delta\mathbf{q} + \mathbf{E}\delta\mathbf{u} + \nu, \tag{1c}$$

$$\delta\mathbf{z} = \mathbf{F}_v\delta\mathbf{v} + \mathbf{F}_q\delta\mathbf{q} + \mathbf{G}\delta\mathbf{u}. \tag{1d}$$

The Kalman filter integrates ~~these equations over time~~ the linearized model by first predicting the system ~~state variables~~ states and their uncertainties, and then correcting ~~(innovating) these estimates~~ these predictions using the available measurements ~~, considering their associated uncertainties. Since~~ and their associated noise characteristics. Because the underlying model is linearized, the ~~non-linear~~ nonlinear values of all quantities are ~~obtained~~ recovered by adding the perturbations to the ~~reference equilibrium conditions. For example, the generalized displacements are computed as~~ corresponding equilibrium values, e.g. $\mathbf{q} = \mathbf{q}_0 + \delta\mathbf{q}$, and ~~the same holds~~ analogously for all other vectors ~~appearing~~ in Eqs. (1).

Equations (1a) ~~are the~~ represent the (noise-free) kinematic relations, ~~which are assumed to be exact and not affected by noise.Equations~~while Eqs. (1b) express the dynamic equilibrium ~~of the system, affected by the process noise ω, where~~ affected by process noise $\boldsymbol{\omega}$, with $\mathbf{M}$, $\mathbf{C}$, $\mathbf{K}$, and $\mathbf{U}$ ~~are, respectively,~~ denoting the mass, damping, stiffness, and control matrices. ~~Finally, Eqs.~~Equations (1c) and (1d) ~~represent~~ give the linearized output ~~equations~~ relations for $\mathbf{y}$ and $\mathbf{z}$, respectively. ~~The~~ All noise terms are assumed ~~to be zero mean~~ zero-mean and uncorrelated (Grewal and Andrews, 2014).

~~It should be noted that the equilibrium conditions are, in general, periodic. As a result, the entries of the~~ Although a standard linear Kalman filter would be sufficient for the present linearized state–space model, we adopt the unscented Kalman filter (UKF) implementation of MATLAB (Wan and Van Der Merwe, 2000; The MathWorks, Inc., 2022). This choice is motivated by anticipated future extensions to nonlinear filter-internal models. While the use of the UKF is therefore not strictly necessary in the present linear case, it remains fully applicable to linear systems, albeit with somewhat higher computational cost compared to a standard linear Kalman filter.

Because the equilibrium conditions are generally periodic, the matrices associated with rotating quantities ~~– as well as the associated –~~and the corresponding states, inputs, and ~~outputs – depend on time through the time-dependent azimuthal position of the rotor~~ outputs– depend on the rotor azimuth. To avoid ~~working~~ dealing with periodic systems, this ~~dependency is eliminated by averaging throughout a complete rotor~~ dependence is removed by averaging over one full revolution.

The present implementationconsiders 9 DOFs in the definition of the In the present implementation, the filter-internal dynamics. Accordingly, model includes 9 DOFs, and the generalized displacement vector is defined as

$$\mathbf{q} = \left\{ d_T^{FA}, d_T^{SS}, \psi, d_{B1}^F, d_{B2}^F, d_{B3}^F, d_{B1}^E, d_{B2}^E, d_{B3}^E \right\}^T, \tag{2}$$

where d_T^{FA} and d_T^{SS} are the tower FA and SS deflections, respectively, ψ is the rotor azimuthal position, while d_{Bi}^F and d_{Bi}^E are respectively the flapwise and edgewise DOFs of the ith blade. The associated velocities are $\mathbf{v} = \dot{\mathbf{q}}$.

The input vector $\mathbf{u}$ contains 8 entries and it is defined as

$$\mathbf{u} = \left\{ V, \alpha, \gamma, \theta_1, \theta_2, \theta_3, \theta_{\text{coll}}, Q_{\text{gen}} \right\}^T, \tag{3}$$

where V is the wind speed, α is the vertical power-law shear exponent, γ is the the yaw misalignment angle, θ_i is the total blade pitch angle of the total pitch of blade ith blade, θ_{coll} is the collective blade pitchanglethe collective pitch, and Q_{gen} indicates the generator torque. Individual pitch control adds to the ith blade an extra amplitude $\theta_i - \theta_{\text{coll}}$ with respect to the collective valueintroduces a blade-specific pitch component $\theta_i - \theta_{\text{coll}}$, whereas $\theta_i = \theta_{\text{coll}}$ when only collective pitch is used. Notice that the input to the model not only considers the control inputs (i.e., quantities commanded by active. The input vector thus includes not only control commands from the on-board control system) but also includes exogenous terms due to the ambient conditionscontroller but also exogenous terms associated with the ambient inflow. The present inputs are relevant to the linearization performed set of inputs corresponds to those used for linearization in OpenFAST (Jonkman et al., 2018; NREL Forum), although other codes might use different quantities; for example, we note the presence of the vertical shear but not of the horizontal one; other simulation tools may use different inflow descriptors (e.g., including horizontal shear).

It is assumed We assume that a biaxial accelerometer measures accelerationsat the tower topprovides tower-top accelerations, an encoder measures the rotor speed, and load measurements are available for each blade in the form of blade root loads are available in flapwise and edgewise bending moment components. Accordingly, the directions for each blade. The output vector $\mathbf{y}$contains 9 entries and it , therefore, contains nine components and is defined as

$$\mathbf{y} = \left\{ \ddot{d}_T^{FA}, \ddot{d}_T^{SS}, \dot{\psi}, m_{B1}^F, m_{B2}^F, m_{B3}^F, m_{B1}^E, m_{B2}^E, m_{B3}^E \right\}^T. \tag{4}$$

The FA and SS tower top accelerations are tower-top accelerations are denoted by $\ddot{d}_T^{FA}$ and $\ddot{d}_T^{SS}$, respectively, the . The rotor angular speed is $\dot{\psi} = \Omega\dot{\psi} = \Omega$, while the flapwise and edgewise bending components for the ith bladeare noted moments of blade i are indicated by m_{Bi}^F and m_{Bi}^E, respectively.

The model is completed by the definition of defining additional to-be-estimated quantities collected in the vector $\mathbf{z}$, which , however, do not participate in the filter innovation step. This is because of two possible exclusion may occur for two reasons:

- the digital shadow operates as a virtual sensor , as measurements of these quantities are not available through physical sensors (because of for quantities that are not physically measured due to technical or economic reasons)constraints;
- the digital shadow supports a condition monitoring systemthat compares predictions with measurements in order condition-monitorin system, where predicted and measured values are compared to detect anomalies and or faults.

Both ~~of these~~ scenarios are illustrated later in this work. ~~Here the~~ In the present implementation, the $\mathbf{z}$ outputs ~~are represented by the~~ include the tower-base bending moment components m_{TB}^{FA} and m_{TB}^{SS} ~~of the bending moment at tower base and by the components~~ $m_{Bi-15\%}^{F}$, as well as the flapwise and edgewise bending moments $m_{Bi-15\%}^{F}$ and ~~$m_{Bi-15\%}^{E}$ of the bending moment at~~ $m_{Bi-15\%}^{E}$ at the 15% ~~span of each blade ; however, other choices are clearly possible, depending on need~~blade span. Other quantities could be selected depending on the specific application.

2.2 Model scheduling

To be usable in practice, the filter-internal model is scheduled as a function of a small set of parameters $\mathbf{s}$, ~~chosen to capture~~ selected to characterize the equilibrium operating condition about which the linearization is performed. ~~As a result~~Consequently, all matrices ~~appearing~~ in the state-space ~~model expressed by~~ representation of Eqs. (1) depend on $\mathbf{s}$. For example, ~~considering~~ the mass matrix ~~,~~ becomes $\mathbf{M} = \mathbf{M}(\mathbf{s})$, and ~~the same holds~~ similarly for all other ~~matrices. Similarly, all~~ system matrices. The equilibrium values of the states, inputs, and outputs ~~at the equilibrium condition depend on~~ also vary with $\mathbf{s}$~~. For example, considering~~ ; for instance, the generalized displacements ~~,~~ satisfy $\mathbf{q}_0 = \mathbf{q}_0(\mathbf{s})$, ~~and the same holds for all other~~ with analogous relations holding for the remaining vectors.

The vector of scheduling parameters is defined as

$$\mathbf{s} = \{V, \alpha, k_h, \gamma\}^T. \tag{5}$$

The first two entries ~~express~~ capture the dependency of the model ~~coefficients and equilibrium reference values~~ on the ambient conditions through the wind speed V and the vertical power-law shear exponent α. The third entry is the ~~linear horizontal shear k_h, on account of the possible presence of impinging wakesshed by upstream turbines. The fourth entry is γ,~~ horizontal shear k_h, accounting for wakes, and the fourth is the yaw misalignment ~~angle, included here to support wake-steering conditions for wind farm control~~γ, relevant for wake steering.

The ~~purpose of the scheduling vector of parameters is to make the model (and , hence, the filter) aware of the~~ scheduling vector enables the model and filter to remain aware of operating conditions that ~~affect the turbine response; these effects~~ would otherwise be lost ~~when moving from the full non-linear model to its linearization.~~

after linearization. The non-linear model is linearized at a ~~preselected~~ set of discrete ~~values of~~ $\mathbf{s}$ ~~, chosen to cover the entire range of operative and ambient conditions of the machine. The~~ values spanning the full operational and ambient range, and the corresponding matrices and equilibrium ~~states, inputs and outputs~~ quantities are stored in look-up tables (LUTs). ~~To express the dependency of the model on the linearization point, at run time, the current value of the scheduling vector~~ During operation, $\mathbf{s}$ is estimated ~~at each time instant by dedicated observers as explained in~~ in real time (Sect. 2.3), and the model matrices ~~are interpolated accordingly. The equilibrium values of states, inputs and outputs are similarly interpolated , which allows for the transformation of the filter-predicted incremental values into their~~ and equilibrium values are interpolated accordingly, allowing the incremental filter predictions to be mapped back to the non-linear ~~corresponding~~ physical quantities.

2.3 Observers

As previously explainednoted, the filter-internal model coefficients are is scheduled with respect to the parameters sthat capture the current operating conditions. These parameters are chosen here , here chosen as the wind speed, the vertical and horizontal shears, and the misalignment angle.

These quantities are estimated at each instant of in real time during operation and used to inform update the filter-internal model of the current conditionsaccordingly. The present sequential implementation – where observers feed information setup –where observers supply s to the Kalman filter – is clearly not the only option. Alternatively, one could have included the estimation of s in an expanded Kalman filter. The sequential approach was chosen here purely for simplicityand because legacy implementations of the filter– is adopted for simplicity, as legacy observers were already available (Hoghooghi et al., 2024). However, an augmented Kalman filter could alternatively estimate s directly.

Regarding the misalignment, we note that its actual value can differ significantly Since the actual misalignment can differ substantially from the commanded one. Therefore, here, we prefer to estimate , γ through is estimated via an observer rather than using the values requested by the on-board controller taken from the controller demand.

2.3.1 Simple wind speed observer

A rotor-equivalent wind speed is obtained by inverting the expression of the power coefficient:

$$C_p(\theta_{\text{coll}}, \lambda) = \frac{Q_{\text{aero}}\Omega}{0.5\rho A V^3}, \tag{6}$$

where $\lambda = \Omega R/V$ $\lambda = \Omega R/V$ is the tip-speed ratio, R is the rotor radius, $A = \pi R^2$ $A = \pi R^2$ is the rotor swept area, Q_{aero} is the aerodynamic torque, and ρ indicates is the air density. The power coefficient C_p is computed by executing dynamic simulations with obtained from dynamic simulations of the full aeroservoelastic turbine model in constant wind speeds model in steady wind conditions for a reference density ρ_{ref}. Sufficient time is allowed for the transient response to subside, and afterwards, After transient effects decay, the response is averaged over a few several rotor revolutions to compute the relevant extract the steady-state quantities. The results are stored in values. These results populate a LUT, yielding an expression providing a mapping for the rotor-equivalent wind speed as a function of pitch, rotor speed, aerodynamic torque, and density:

$$V = \text{LUT}_{C_p}(\theta_{\text{coll}}, \Omega, Q_{\text{aero}}, \rho/\rho_{\text{ref}}). \tag{7}$$

At run time, the LUT is used to obtain provides an estimate V_E of the rotor-equivalent wind speed. The current pitch setting θ_{coll} and rotor speed Ω are measured by the corresponding read from on-board sensors. The aerodynamic torque is computed as $Q_{\text{aero}} \approx Q_{\text{gen}} + J\dot{\Omega}$ $Q_{\text{aero}} \approx Q_{\text{gen}} + J\dot{\Omega}$, where Q_{gen} is the measured generator torque , and the angular acceleration and $\dot{\Omega}$ is obtained by numerically differentiating the rotor speed, Ω, with J being the rotor inertia. Finally, Air density ρ is computed using via the gas law from using the measured temperature.

2.3.2 Shear and misalignment observers

The ~~estimation of the~~ horizontal and vertical shears~~and of~~ , as well as the wind misalignment~~is obtained by the "~~, are estimated using the "rotor as a sensor~~" technology (see Kim et al. (2023); ? and references therein). This method~~ " approach (Kim et al., 2023; Bertelè et al., 2024), which exploits the fact that ~~each of~~ these inflow characteristics ~~leaves a specific trace in the load response of a wind turbine. Leveraging this fact, one can then "invert" the measured response to infer these inflow quantities~~ imprint distinctive signatures in the blade load response. By inverting these signatures, the corresponding inflow quantities can be inferred.

~~In this work, we use a version of the rotor as a sensor based on load harmonic amplitudes (Kim et al., 2023; ?). In a nutshell, the estimator is formulated~~ Here, we adopt the harmonic-amplitude-based formulation of the rotor-as-a-sensor method (Kim et al., 2023; Bertelè et al., 2024). The estimator is written as

$$c_E = NN(\mathbf{p}, \mathbf{i}_M), \tag{8}$$

where c_E is ~~an estimated wind inflow characteristic (either the vertical power-law shear coefficient~~ the estimated inflow quantity (either α, ~~the horizontal linear shear coefficient~~ k_h, or ~~the yaw misalignment angle~~ γ), $NN(\cdot,\cdot)$ is a single-output NN with ~~free~~ parameters $\mathbf{p}$, and $\mathbf{i}_M$ is ~~a~~ the vector of measured ~~NN~~ inputs. A ~~different~~ separate NN is used for each ~~one~~ of the three inflow parameters~~of interest~~. The input vector is defined as ~~$\mathbf{i}_M = \{\mathbf{m}^T, V, \rho\}^T$~~ $\mathbf{i}_M = \{\mathbf{m}^T, V, \rho\}^T$, where $\mathbf{m}$ ~~is a vector of harmonic amplitudes of the blade loads. For~~ collects the relevant blade-load harmonics. Since the estimation of shears and misalignment ~~, it is enough to limit the harmonics to the one per rev (~~only requires 1P ~~) components (Kim et al., 2023; ?). Accordingly, vector $\mathbf{m}$ is defined as~~ content (Kim et al., 2023; Bertelè et al., 2024), we define

$$\mathbf{m} = \{m_{1c}^{OP}, m_{1s}^{OP}, m_{1c}^{IP}, m_{1s}^{IP}\}^T, \tag{9}$$

where ~~the~~ subscripts $(\cdot)_{1c}$ and $(\cdot)_{1s}$ ~~respectively indicate~~ denote 1P cosine and sine terms, ~~while the~~ and superscripts $(\cdot)^{OP}$ and $(\cdot)^{IP}$ ~~indicate out~~ refer to out- and in-plane load components~~, respectively. The out and in-plane load components are referred to the rotor disk, and they are~~ . These components are obtained by transforming the measured flapwise and edgewise ~~components measured by the blade-attached sensors~~ loads to the rotor disk frame based on the current blade pitch~~setting~~.

The ~~present implementation is based on a~~ NNs are simple single-hidden-layer feed-forward ~~neural network~~ models with sigmoid activation~~functions. The free network parameters~~ . Parameters $\mathbf{p}$ are trained ~~by~~ via backpropagation with Bayesian regularization ~~to reduce the chances of being trapped in local minima (Matlab, 2023; Burden and Winkler, 2009) . Training is based on simulations conducted with the full aeroelastic model of the turbine using OpenFAST~~ (Matlab, 2023; Burden and Winkler, 2009) using simulations from the full OpenFAST aeroelastic model (OpenFAST, 2024). At each ~~time~~ simulation step, the inflow quantities ~~(shears and misalignment)~~ are extracted from the TurbSim ~~(TurbSim, 2023) turbulent flow field~~ field (TurbSim, 2023) by best-fitting over the rotor disk~~area. Load harmonics are obtained from the blade root sensors via the Coleman-Feingold~~ , and load harmonics are computed via the Coleman–Feingold transformation (Coleman and Feingold, 1958) and ~~then filteredto remove any remaining spurious noise.~~

~~At run time~~subsequently filtered. During operation, Eq. (8) ~~is used to produce estimates of the inflow quantities based on~~ provides real-time estimates of α, k_b, and γ using the measured load harmonics, ~~on the current~~ the rotor-equivalent wind speed from Eq. (7), and ~~on~~ air density ρ.

2.4 Model error correction

In ~~general~~practice, some mismatch between the plant and the filter-internal model is ~~to be expected~~unavoidable, and this ~~will invariably affect~~ affects the performance of the digital shadow. ~~The effects of model mismatches~~ Such discrepancies can be mitigated ~~in various ways, such as by the tuningof the model parameters, by the~~ through model-parameter tuning, dynamic data-driven ~~adaption of the model (Anand and Bottasso, 2023; Bottasso et al., 2006), by the correction of biases~~ model adaptation (Anand and Bottasso, 2023; Bottasso et al., 2006), bias-correction strategies (Chui and Chen, 1999; Drécourt et al., 2006; Grewal and Andrews, 2008), or by adapting the process noise ~~term to capture the effects of unmodelled physics , among others (Branlard et al., 2020a). Here, we explore two methods~~to account for unmodelled physics (Branlard et al., 2020a). In this work, we focus on two approaches: a bias-correction ~~approach~~ method and a data-driven correction ~~limited~~ applied only to the output equations.

2.4.1 Bias correction

First, we ~~consider the correction of biases, intended~~ address bias correction (BC), interpreted as additive errors in the model. To this end, the filter-internal model ~~expressed by~~ of Eqs. (1) is modified as

$$\dot{\delta\mathbf{q}} = \delta\mathbf{v}, \tag{10a}$$

$$\dot{\delta\mathbf{v}} = -\mathbf{M}^{-1}(\mathbf{C}\delta\mathbf{v} + \mathbf{K}\delta\mathbf{q} + \mathbf{U}\delta\mathbf{u} + \mathbf{f}_0 + \omega), \tag{10b}$$

$$\dot{\mathbf{b}} = \omega_b, \tag{10c}$$

$$\delta\mathbf{y} = \mathbf{D}_v\delta\mathbf{v} + \mathbf{D}_q\delta\mathbf{q} + \mathbf{E}\delta\mathbf{u} + \mathbf{b} + \nu, \tag{10d}$$

$$\delta\mathbf{z} = \mathbf{F}_v\delta\mathbf{v} + \mathbf{F}_q\delta\mathbf{q} + \mathbf{G}\delta\mathbf{u}. \tag{10e}$$

With respect to Eqs. (1), the model is modified to include two corrections.

The first ~~is represented by~~ correction term is the static force $\mathbf{f}_0$, which induces a steady extra deflection in the generalized displacements ~~, meant to correct possible~~ to compensate model biases. As ~~for all other terms in the model , also~~ with all model terms, $\mathbf{f}_0$ ~~is assumed to depend~~ depends on the operating condition through the ~~vector of scheduling parameters~~ scheduling vector $\mathbf{s}$.

A second ~~modification is obtained by introducing the~~ correction is the additive term $\mathbf{b}$ in the output equation (Eq. ~~(~~10d), ~~on account of possible biasesin the sensors. Following a standard bias correction approach~~ which accounts for sensor biases. Following standard practice (Chui and Chen, 1999; Drécourt et al., 2006; Grewal and Andrews, 2008), ~~the extra term~~ $\mathbf{b}$ is promoted to a ~~new state variable~~ state undergoing a random walk ~~excited by the~~ driven by process noise ω_b, as ~~expressed by~~ in Eq. (10c).

It should be noted that the two correction terms may compete with each other, and it might not always be possible to disentangle the effects of one from the effects of the other. In fact, Because $\mathbf{f}_0$ and $\mathbf{b}$ can be collinear, their effects may not be uniquely separable: a correction on the generalized displacements performed by $\mathbf{f}_0$ will in turn correct the outputs through the $\delta\mathbf{q}$ term in Eq. (10d), eventually affecting $\mathbf{b}$. To cope with the possible collinearity of these two correctionsmitigate this, $\mathbf{f}_0$ is first calibrated by neglecting with $\mathbf{b}$ from the model. Once disabled; once suitable values for $\mathbf{f}_0$ for varying $\mathbf{s}$ have been obtained, then $\mathbf{f}_0$ is frozen and the bias $\mathbf{b}$ is activated in the filter. This two-step process is demonstrated lateron. In the interest of . For simplicity, one can instead neglect may omit $\mathbf{f}_0$ and only use the extra entirely and rely only on $\mathbf{b}$states, implicitly accepting that the displacements might be in error. Additionally, one can iterate between calibrating $\mathbf{f}_0$ and $\mathbf{b}$, adjusting both corrections to achieve better accuracy, accepting possible displacement errors. Iterative tuning of both terms is also possible.

It is worth mentioning that the tuning of the model is performed Finally, tuning is based solely on the measured outputs $\mathbf{y}$, as in general measurements of the states or biases are not availablesince neither states nor sensor biases are directly measurable.

2.4.2 A posteriori error correction for condition monitoring applications

Next, we consider a case relevant to CM applications. In this scenario , CM-oriented scenario in which the digital shadow is tasked with predicting the behavior of some predicts selected quantities of interest . However, measurements are available for these same quantities while measurements of the same quantities are also available at run time. A CM system can then exploit this redundancy by comparing compare predictions and measurements in order to detect faults or anomalies. Clearly, for such a system to work in an effectivemannerFor this redundancy to be effective, the digital shadow predictions must be in very close agreement with the measurements in all nominal operating must closely match the measured behavior under nominal conditions. In general, such a close match is not possible by the use of the model expressed by practice, the baseline model of Eqs. (1) cannot typically achieve such accuracy.

To achieve the desired accuracy between predictions and measurementsimprove agreement, the linearized output equations for $\mathbf{z}$ (Eq. 1d) are augmented with a correction term ~~ϵ~~ϵ:

$$\delta\mathbf{z} = \mathbf{F}_v\delta\mathbf{v} + \mathbf{F}_q\delta\mathbf{q} + \mathbf{G}\delta\mathbf{u} + \epsilon. \tag{11}$$

For complete generality, the error correction term is assumed to depend on the states $\delta\mathbf{q}$ and $\delta\mathbf{v}$, inputs $\delta\mathbf{u}$ and scheduling parameters $\mathbf{s}$, and it is approximated using a neural network:

$$\epsilon = NN_\epsilon(\mathbf{p}_\epsilon, \mathbf{s}, \delta\mathbf{q}, \delta\mathbf{v}, \delta\mathbf{u}), \tag{12}$$

where $\mathbf{p}_\epsilon$ are the free network parameters.

Note that this approach does not attempt to correct the system governing dynamics expressed by modify the governing dynamics in Eq. (1b). This means that Consequently, the filtered states will , in general, not precisely match the true plant states (which, typically , are also not known) . Nonetheless, this approach can still deliver generally not coincide with the true (and typically unknown) plant states. However, accurate estimates of the outputs of interest $\mathbf{z}$ when can still be achieved by training the correction term is trained to learn the measured outputs ~~$\mathbf{z}_M$~~$\mathbf{z}_M$.

Here againAs before, a simple single-hidden-layer feed-forward neural network is found to give the necessary NN provides sufficient accuracy. Training is based on backpropagation (Matlab, 2023). Weibull weighting is used to improve performance in performed by backpropagation (Matlab, 2023), with Weibull weighting applied to emphasize the most probable operating conditions (Bangalore et al., 2017; Surucu et al., 2023; Anand and Bottasso, 2023).

3 Results

3.1 Simulation-based results

First, we investigate the performance of the proposed digital shadow framework in a simulation environment, We assess the digital shadow in simulation using the IEA-3.4-130-RWT -130 reference wind turbine (IEA3.37MW, 2023) as (RWT) (IEA3.37MW, 2023) implemented in OpenFAST (OpenFAST, 2024). The complete aeroelastic model was linearized for wind speeds ranging from from 5 to 25 with increments of 1 , power-law $\mathrm{m\,s^{-1}}$, vertical shear exponents spanning from from 0 to 0.48with increments of 0.12, horizontal shears ranging , horizontal shear from -0.1 to $0.1$with increments of 0.1, and at , and yaw misalignments of $0°$ and $-30°$. The filterwas , implemented in MATLAB(The MathWorks, Inc., 2022), and its execution on a standard single-CPU laptop took of the order of (The MathWorks, Inc., 2022), required about 6 minutes for a 10-minute physical-time simulation at a step frequency of to simulate 10 minutes of physical time at 100 Hz on a standard single-CPU laptop.

Turbulent flow inflow fields were generated with TurbSim(TurbSim, 2023), spanning wind speeds varying in the range (TurbSim, 2023) for wind speeds of 5–11 , with a vertical power-law $\mathrm{m\,s^{-1}}$, a vertical shear exponent of 0.20.2, and turbulence intensities (TIs) of 6% and 18%. According to standards, simulations were conducted for a duration of 10 minutes and repeated for 6 distinct Simulations followed standard 10-minute runs with six random seeds. Gaussian noisewas added to each measurement signal to account for typical uncertainties affecting SCADA sensors (Branlard et al., 2020b, a), with the noise level set at , equal to 10% of the standard deviation of each signal. Damage equivalent , was added to emulate SCADA sensor uncertainties (Branlard et al., 2020b, a). Damage-equivalent loads (DELs) were computed by rainflow counting(Natarajan, 2022) . via rainflow counting (Natarajan, 2022). Unless stated otherwise, all results presented in this section refer to the representative operating condition described below in Sect. 3.1.1.

While various aspects of the digital shadow formulation are significant, the selection of the Estimation accuracy depends strongly on the choice of process and measurement covariance matrices, as well as the filtering of measurements, can strongly impact the accuracy of the estimates (Branlard et al., 2020a). The measurement covariance was based on the expected noise affecting the measurements. The process noise covariance was empirically tuned by a trial and error process to improve the accuracy of the estimates (Branlard et al., 2020a).The tuned covariance did not exhibit a significant dependence on wind speed (Branlard et al., 2020a). Measurement covariance reflected expected sensor noise, while process covariance was tuned empirically. The resulting values showed little dependence on the operating condition and delivered consistent performance across all cases.

3.1.1 Representative example and input data

To illustrate the digital shadow workflow and clarify the associated input data, we provide a brief summary of a representative simulation case that is used repeatedly throughout Sect. 3.1. The reference example corresponds to a single IEA 3.4-130 RWT (IEA3.37MW, 2023) operating in Region II at a mean wind speed of 7 $\mathrm{m\,s^{-1}}$, with a vertical power-law shear exponent of 0.2 and TIs of 6% and ~~turbulence, eventually delivering a consistent performanceacross all considered conditions.~~18%. Turbulent inflow fields are generated with TurbSim (TurbSim, 2023) using standard 10-minute realizations and six random seeds.

The digital shadow receives as inputs the measured rotor speed, generator torque, selected blade-root and tower load measurements, and air density (assumed known). Gaussian noise with a standard deviation equal to 10% of each signal standard deviation is superimposed to emulate SCADA sensor uncertainty. These measurements are processed by the filter to estimate rotor-equivalent wind speed, vertical and horizontal shears, structural states, and fatigue-relevant load quantities. This representative case is used in Figs. 2–5 to demonstrate observer performance, bias-correction behavior, as well as state and load estimation accuracy before extending the analysis to waked and yaw-misaligned turbines in Sect. 3.1.5.

3.1.2 Estimation of wind speed and shears

We ~~start by verifying~~ first assess the accuracy of the ~~estimates of~~ estimated wind speed and shear ~~, which are~~ used to schedule the model coefficients. ~~Reference (ground truth) values were obtained at each instant of time~~ Ground-truth values were extracted directly from the TurbSim longitudinal ~~components of the~~ wind field: ~~speed was obtained by averaging over the rotor disk, while shears by interpolating over the same rotor disk area~~ the rotor-average wind speed was computed by disk-averaging, while vertical and horizontal shears were obtained by fitting a power law ~~in the vertical direction~~ and a linear ~~function in the horizontal one~~profile over the rotor disk, respectively.

Figure 2 compares the reference rotor-average ~~wind~~ speed (dashed blue~~line~~) with the estimated rotor-equivalent wind speed V_E from Eq. (7) (solid red~~line) for one of the simulations conducted in regionII at a wind speed of 7 $\mathrm{m\,s^{-1}}$ and TI equal to~~) for a representative region II simulation at 7 $\mathrm{m\,s^{-1}}$ and TIs of 6% (Fig. 2a) and 18% (Fig. 2b). ~~For the calculation of the estimated rotor-equivalent wind speed, the~~ To compute V_E, rotor speed and torque ~~signals~~ were low-pass filtered ~~using~~ with a fifth-order Butterworth filter with a ~~−3 dB~~ -3 dB cutoff frequency of 8 rpm (Schreiber et al., 2020b), ~~in order to eliminate higher-frequency~~ removing high-frequency turbine dynamics and measurement noise.

For the same operating condition, Fig. 2c ~~shows time histories of~~ compares the reference power-law vertical shear (dashed blue~~line) and its estimate obtained with~~) with its estimate from Eq. (8) (solid red~~line~~). Figure 2d ~~displays a time history of~~ shows the reference linear horizontal shear ~~(dashed blue line) and of its estimate from Eq. (8) (solid red line) for a wind turbine in full-waked conditions (as described later in~~ and its estimate for a fully waked turbine (Sect. 3.1.5)~~. We demonstrate the behavior of the horizontal observer in this condition~~ , a case selected because wake meandering ~~creates visible changes in the shear at the impinged turbine, whereas only very modest horizontal shear changes are~~ induces clear horizontal shear fluctuations, unlike the modest variations typically observed in ~~TurbSim ambient~~ ambient TurbSim flow fields.

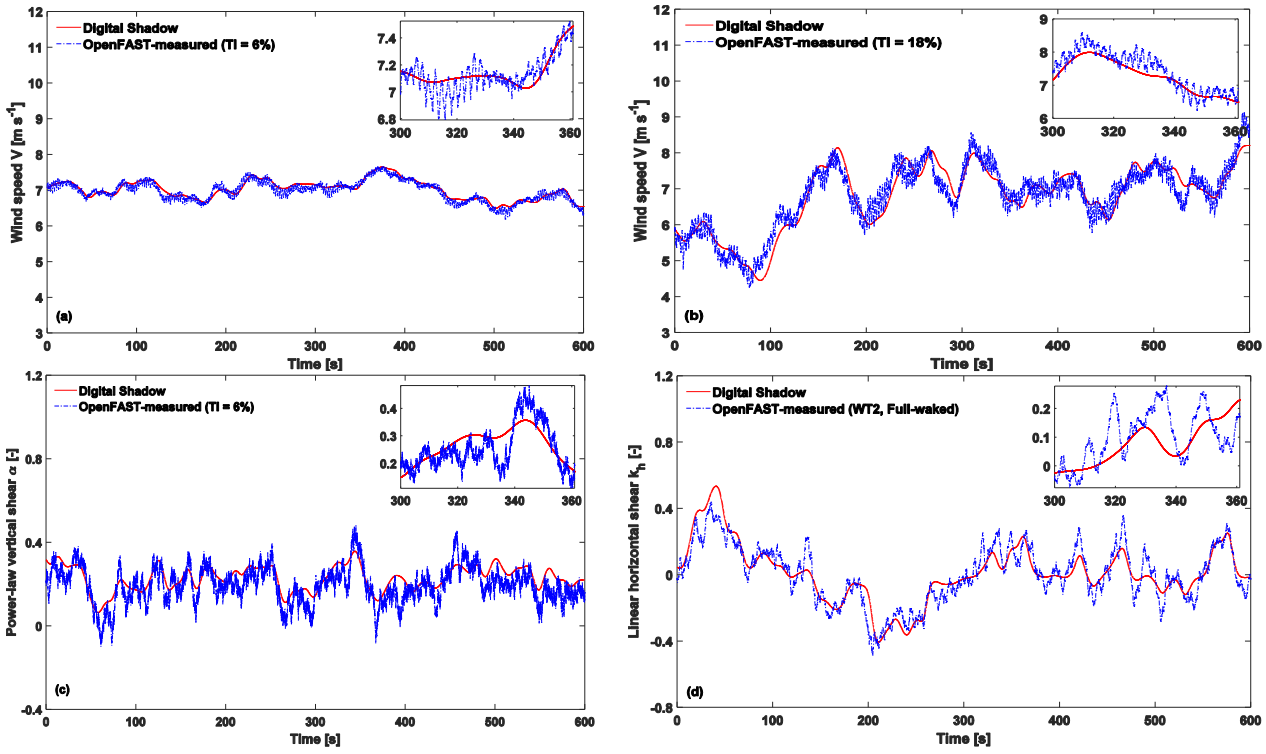

Figure 2. Time histories of the rotor-average wind speed from TurbSim and from Eq. (7) at a wind speed of 7 $\mathrm{m\,s^{-1}}$ and at TIs of 6% **(a)** and 18% **(b)**, respectively. **(c)**: time histories of the power-law vertical shear from TurbSim and from Eq. (8), a wind speed of 7 $\mathrm{m\,s^{-1}}$, and TI equal to 6%. **(d)**: time histories of the linear horizontal shear from TurbSim and from Eq. (8) for the downstream turbine in full-waked conditions (see Sect. 3.1.5). Reference results from TurbSim: dashed blue line; estimates: solid red line.

~~For the calculation of shears, the load harmonics were computed via the Coleman–Feingold transformation(Coleman and Feingold, 1958) from the corresponding measured signals~~Shear estimation relies on load harmonics obtained via the Coleman-Feingold transformation (Cole , followed by low-pass filtering (Bertelè et al., 2021). The ~~shear-observing network is also fed with the estimated~~ network also receives the estimated rotor-equivalent wind speed V_E ~~obtained~~ from Eq. (7) and ~~with~~ the air density (~~here assumed to be known, and therefore not estimated~~assumed known).

~~In~~ Across all cases, the ~~estimates track the ground-truth values reasonably well , although they fail to capture some of the higher frequency~~ observers track the ground truth reasonably well but miss some higher-frequency content. This ~~is due to the fact that the rotor-equivalent wind speed is estimated through the response of the turbine, which is smoothed by the large inertia of the rotor and the presence of the control system. Similarly,~~ loss is expected, as V_E is inferred from turbine response –filtered by rotor inertia and control action– while the shear observers ~~are driven by load harmonics , which here again entail some filtering of the higher frequency content of the~~ rely on load harmonics that similarly smooth the blade response. ~~Considering that~~ Because these quantities are used ~~for scheduling (i.e., interpolating) the system matrices and reference~~ solely to schedule

(interpolate) the model matrices and equilibrium conditions, ~~the absence of some of the highest frequency components is probably an advantage more than a deficiency~~omitting high-frequency components is arguably beneficial.

Over the entire range of simulations, the average absolute ~~error was found to be~~ errors were 2.4% for wind speed, 14.5% for the vertical power-law shear exponent, and 11.1% for the linear horizontal shear. ~~Furthermore, the average error for the mean yaw misalignment in the wake steering scenarios (described later in~~ In wake-steering scenarios (Sect. 3.1.5), the mean yaw-misalignment estimation error was 14.5%.

3.1.3 Performance of the bias correction approach

~~To evaluate~~ To assess the BC approach ~~described in~~ of Sect. 2.4.1 and ~~to analyze the behavior~~ examine the roles of the two correction terms, we ~~employed the same individual turbine operating~~ used the same turbine in a clean low-TI inflow ~~that was used~~ as in Sect. 3.1.2. ~~Initially, the~~ BC terms were ~~switched off, yielding the baseline performance~~ initially disabled to establish the baseline of the uncorrected ~~approach~~model. Figure 3a ~~presents time histories of the tower top FA deflection as measured on the OpenFAST model~~ shows tower-top FA deflection from OpenFAST (dashed blue~~line), uncorrected estimates from the~~), the uncorrected digital shadow (solid red~~line~~), and ~~corrected estimates using the BC approach~~ the BC-corrected estimate (solid yellow~~line) . These results correspond to a wind speed of~~) at 7 $\mathrm{m\,s^{-1}}$ and ~~a turbulence intensity (TI)~~ TI of 6%.

Introducing the static corrective force ~~for the tower FA deflection,~~ $\mathbf{f}_0^{FA}$ ~~,~~ reduces the average absolute error from 16.4% to 2.5%. Figure 3b ~~shows the variation~~ illustrates the dependence of this static force ~~with respect to the wind speed; the force is normalized to one at ratedwind speed~~on wind speed, normalized to unity at rated. Similar analyses were ~~conducted~~ performed for other DOFs ~~,~~ but are omitted ~~here~~ for brevity. ~~It is worth noting that the small deviations observed~~ The remaining discrepancies between the linear and nonlinear models ~~can be attributed to several factors , including~~ stem from factors such as shaft tilt, structural deflections, gravity loads, ~~and slight discrepancies in azimuth angles due to minor differences in rotor speeds between the models (NREL Forum). Additionally, errors in the estimation of~~ small azimuth differences due to slight rotor-speed deviations (NREL Forum), and errors in estimating the scheduling vector s~~contribute to the observed differences between the linear and nonlinear models~~.

~~It is common to observe bias in one or more blade sensors~~ Bias in blade sensors is common (Pacheco et al., 2024). To ~~demonstrate~~ assess the effect of the ~~term~~ $\mathbf{b}$ ~~in the correction of sensor biases (see~~ term for sensor-bias correction (Sect. 2.4.1, Eq. 10c), we artificially ~~introduced a non-zero Gaussian noise in the strain gauge of~~ added Gaussian noise to the blade 1 strain gauge, with a standard deviation of 0.01% and a mean equal to 10% of the mean ~~value of the~~ flapwise bending moment. ~~Results are illustrated in Fig.~~Figure 4a ~~, where the OpenFAST unbiased model measurements are shown as a dashed blueline~~ shows the unbiased OpenFAST measurements (dashed blue) and the biased ~~one as a dashed tealline~~ones (dashed teal). Figure 4b ~~shows how the term~~ illustrates how $\mathbf{b}$ (dashed teal~~line~~) converges to the ~~mean of the artificially added bias in the sensor~~ injected bias (solid yellow~~line~~), effectively correcting the ~~sensor output~~measurement. Figure 4c ~~shows the estimated~~ compares the blade 1 deflection ~~measured on the OpenFAST model without bias~~ from the unbiased OpenFAST model (dashed blue~~line), with artificially introduced bias~~), the biased case (dashed teal~~line~~), and the ~~deflection estimated by the digital shadow using the BC approach~~ BC-corrected digital shadow (solid yellow~~line~~). The average absolute ~~deflection~~ error is 3.61% without the

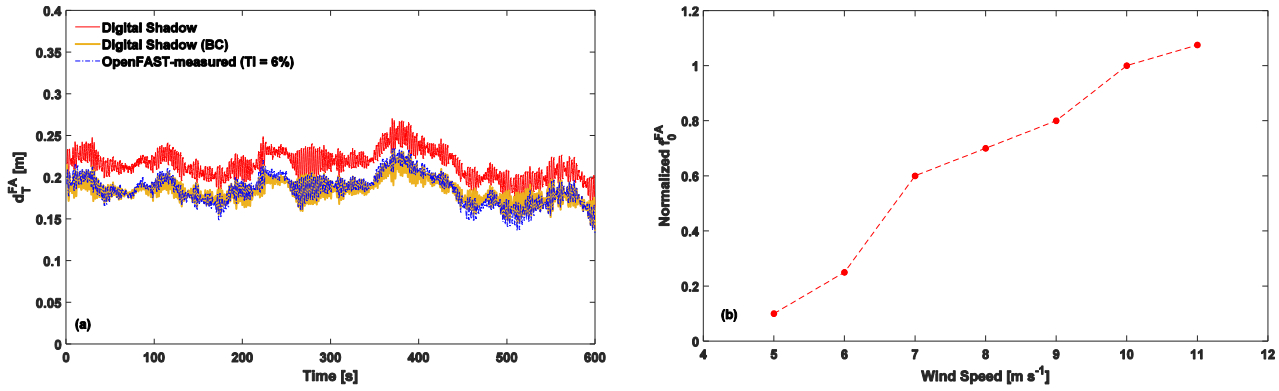

Figure 3. Time histories of tower top FA deflection as measured on the OpenFAST model (dashed blue line), uncorrected estimates from the digital shadow (solid red line), and corrected estimates using the BC approach (solid yellow line) at a wind speed of 7 $\mathrm{m\,s^{-1}}$ and a TI of 6% **(a)**. Variation of the static corrective force $\mathbf{f}_0^{FA}$ for the tower top FA deflection with respect to wind speed **(b)**. The static force is normalized to one at the rated wind speed to highlight relative variations.

artificial bias and 3.67% with ~~the compensated artificial bias, demonstrating~~ compensation, indicating that the correction ~~is able to remove the problem without significant effects on the accuracyof the estimates. We also implemented this method for scenarios where~~ removes the bias without degrading accuracy. Similar performance was obtained when different biases were applied to each blade sensor~~was affected by a different bias, achieving a similar quality in the results~~.

3.1.4 Application to an individual turbine

For the same individual turbine in a clean low-TI inflow ~~shown in~~ of Sect. 3.1.2, Fig. 5a~~through 5d report the time histories of the tower top~~ –d show the tower-top FA and SS displacements ~~,~~ and the blade tip flapwise and edgewise deflections ~~, respectively, as measured on the OpenFAST model~~ measured in OpenFAST (dashed blue~~line~~) and estimated by the digital shadow ~~using~~ with BC (solid yellow~~line). Similarly, Fig.~~). Figures 5e and 5f report the ~~time histories of the~~ tower-base resultant bending moment and ~~of~~ the blade resultant bending moment at 15% ~~blade span, respectively. Figure 5 reports a typical result, which was obtained with one single seed in region II at a wind speed of~~ span. The figure shows a representative case at 7 $\mathrm{m\,s^{-1}}$ and TI ~~equal to 6%~~= 6%. Table 1 ~~gives a more complete overview of the performance of the digital shadow by reporting~~ summarizes the performance across all simulations by listing the average absolute errors~~for all conducted simulations~~.

Results ~~indicate~~ show that the average absolute errors of the estimated turbine states ~~consistently~~ remain below 10% ~~across all conducted~~ for all simulations. DELs were computed for the ~~resultant moment at tower base, noted~~ tower-base resultant moment M_{TB} ~~, and~~ and the blade resultant moment at 15% ~~blade span , noted~~ span $M_{B-15\%}$. ~~The~~ Their average absolute errors ~~for these two quantities are in the range of~~ fall in the 5%–15% range, with standard deviations ~~averaging approximately~~ of about 2.7% for M_{TB} and 4.5% for $M_{B-15\%}$ across all ~~simulation~~ scenarios. As expected, errors ~~are larger for higher~~ increase with TI. The ~~range of the average estimation errors is in line with the findings of~~ overall error levels are consistent

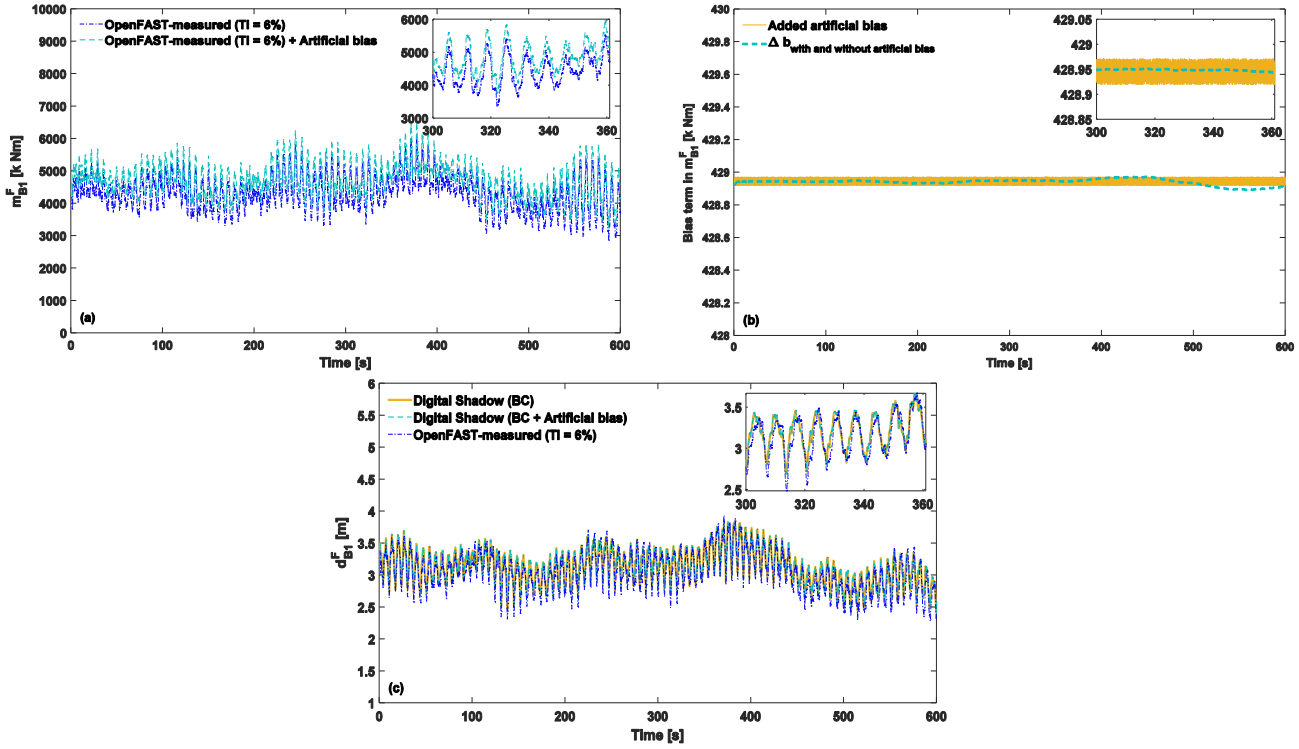

Figure 4. Time histories of blade 1 flapwise bending moment ($\mathbf{m}_F^{B1}$) as measured on the OpenFAST model without bias (dashed blue line) and with artificially introduced non-zero Gaussian noise (dashed teal line) **(a)**. Convergence of the term $\mathbf{b}$ (dashed teal line) to the mean of the artificially added bias (solid yellow line) **(b)**. Time histories of the estimated blade 1 deflection as measured on the OpenFAST model without bias (dashed blue line), with artificially introduced non-zero Gaussian noise (dashed teal line), and as estimated by the digital shadow using the BC approach (solid yellow line) **(c)**. Results correspond to a wind speed of 7 $\mathrm{m\,s^{-1}}$ and a TI of 6%.

Table 1. Average absolute errors for all conducted simulations for clean inflow conditions.

Situation	Avg. estimation error [%]					
	d_T^{FA}	d_T^{SS}	d_B^F	d_B^E	M_{TB} DELs	$M_{B-15\%}$ DELs
No wake, TI=6%	3.1	1.7	3.8	4.4	5.1	12.2
No wake, TI=18%	6.9	3.5	5.6	6.0	6.9	13.0
Average	5.0	2.6	4.7	5.2	6.0	12.6

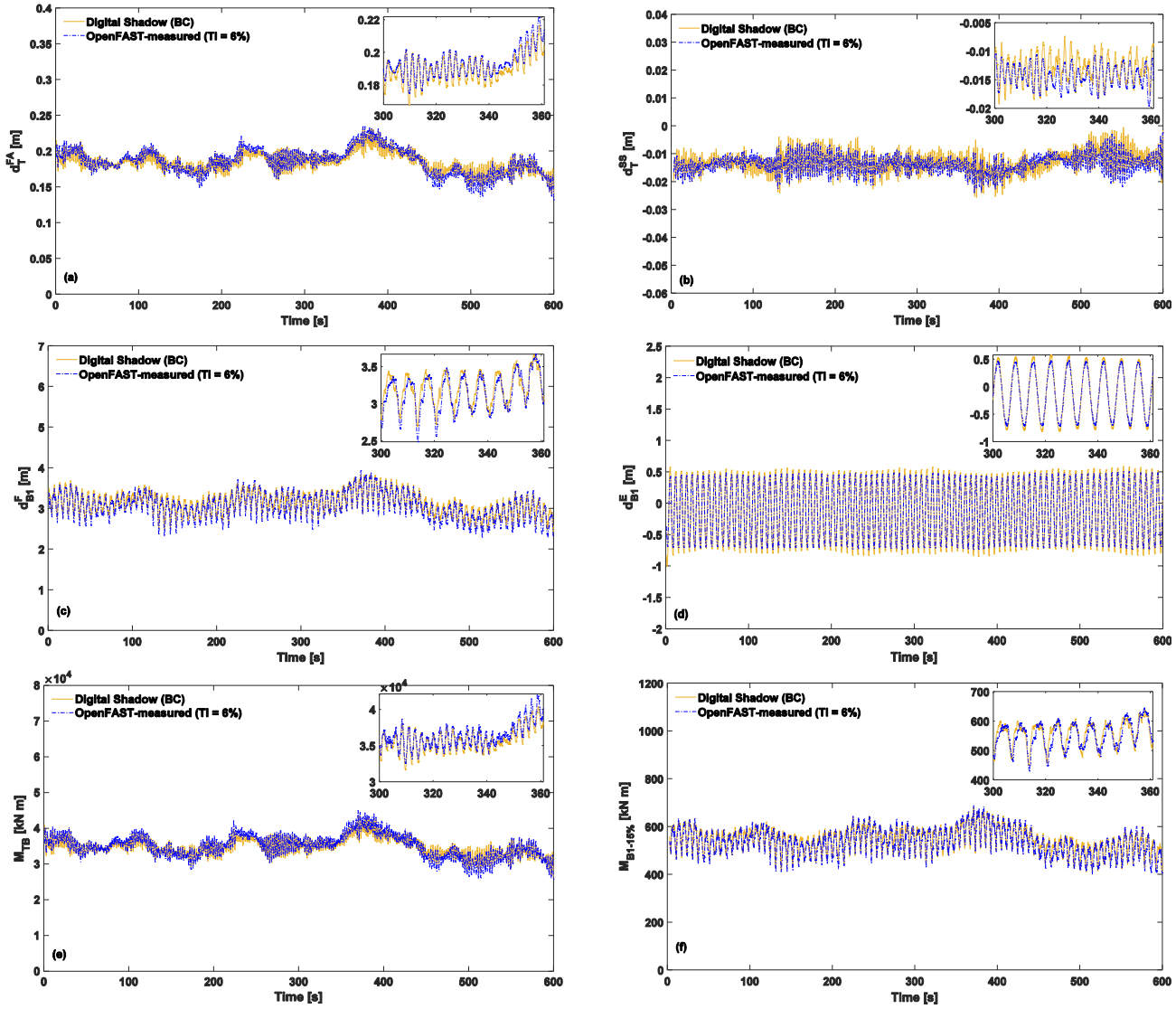

Figure 5. Time histories of tower top FA deflection **(a)**, tower top SS deflection **(b)**, and blade tip flapwise **(c)** and edgewise **(d)** deflections, tower-base bending moment **(e)**, and blade bending moment at 15% blade span **(f)**, as measured on the OpenFAST model (dashed blue line) and estimated by the digital shadow using BC (solid yellow line). A wind speed of 7 $\mathrm{m\,s^{-1}}$ and TI equal to 6% is considered.

with previous studies (Abdallah et al., 2017; Branlard et al., 2020a, b, 2024a), ~~which, however, used a smaller number of~~ although those works relied on fewer DOFs and did not ~~consider~~ include blade dynamics.

3.1.5 Application to waked turbines in a small cluster

To ~~assess the performance of the proposed method in~~ evaluate the method under more complex inflow conditions, ~~simulations were conducted for a small cluster of wind turbines~~ we simulated a small turbine cluster using FAST.Farm (OpenFAST, 2024). The cluster consists of three IEA 3.4-130 ~~RWT turbines~~ RWTs (IEA3.37MW, 2023) arranged in a row ~~, as shown in~~ (Fig. 6~~, and named~~), denoted WT1, WT2, and WT3 ~~, from the upstream to the most downstreamone~~from upstream to downstream.

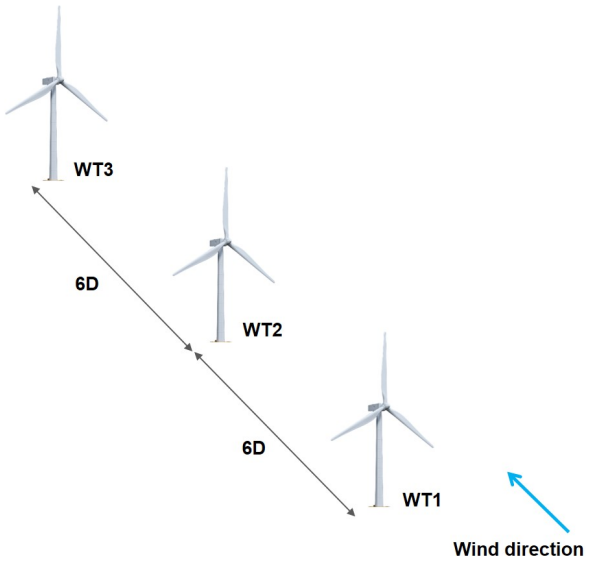

Figure 6. Layout of a small cluster of three IEA 3.4-130 ~~RWT turbines~~RWTs. For all considered cases, the wind direction (indicated by the blue arrow) is parallel to the row of turbines.

Two ~~different scenarios were considered~~scenarios were investigated:

- In the first~~case, the front turbine~~ , WT1 is aligned with the wind ~~direction. The incoming wind is~~ at rated speed ($9.8\ \mathrm{m\,s^{-1}}$) ~~with a turbulence intensity of 6%. As a result, turbine~~ and TI $= 6\%$. WT2 ~~is entirely within~~ lies fully in the wake of WT1, and WT3 ~~is entirely within the wake~~ in the consecutive wakes of WT1 and WT2. The digital shadow is applied to ~~the two downstream wake-affected turbines~~ WT2 and WT3.

- In the second~~case, the~~ , ambient conditions are the same~~as in the first case, but the front turbine~~ , but WT1 is ~~misaligned~~ yawed by $-30°$~~(i.e., pointing to the right when looking upstream) relative to the wind direction. Consequently, turbine~~ . WT2 is then partially waked by WT1, while WT3 is fully ~~within the wake of~~ waked by WT2 and partially ~~in the one of~~

by WT1. The digital shadow is applied to ~~the misaligned front turbine~~ WT1, ~~as well as to the two waked ones~~ WT2, and WT3.

Table 2 ~~presents an overview of~~ summarizes the average absolute errors and ~~the estimated output DELs for the two~~ DEL estimates for both scenarios. For ~~the~~ waked and yawed turbines, ~~the order of magnitude of the average estimation errors in the~~ ~~blade DELs is in line with the errors observed~~ blade DEL errors remain comparable to those obtained in Sect. 3.1.4 for ~~the single turbine operating in a high TI freestream. However, the errors in the tower DELs are somewhat higherin both scenarios. Although the ambient turbulence here is only 6%, these results are~~ a single turbine in high-TI inflow, whereas tower DEL errors are higher. This is consistent with the ~~effects of wake-added turbulence on the impinged turbines. While the errors in the tower DELs~~ added wake turbulence impinging on downstream machines. While tower DEL errors are similar for WT1 ~~in misaligned conditions and for~~ under yaw misalignment and WT2 ~~when partially waked, blade DELs~~ under partial waking, blade DEL errors are larger for ~~the latter. This is~~ WT2, likely due to the complex~~and asymmetrical inflow generated~~ , asymmetric inflow induced by the deflected wake~~on the impacted turbines and the ensuing complex response of the rotor blades~~.

~~Notwithstanding~~ Despite the low ambient ~~turbulence, the errors in the tower DELs~~ TI, tower DEL errors are somewhat larger for the ~~front turbine when it is yawed , compared to the typical errors observed~~ yawed WT1 than for the downstream ~~waked~~ turbines. This ~~is likely due to the complex response of a yawed rotor , which is probably not accurately~~ may reflect the complex rotor aerodynamics in yaw, which are not fully captured by the filter-internal model. ~~In addition, even the blade element momentum (BEM) approach implemented in OpenFAST is not necessarily very accurate in such~~ Moreover, even BEM-based aerodynamics in OpenFAST can be inaccurate in strong yawed-flow conditions (Branlard et al., 2024b), ~~whereas computational fluid dynamics (CFD) and free vortex methods may be able to better render the underlying complex~~ where CFD or free-vortex methods can provide more reliable physics (Boorsma et al., 2018).

Table 2. Average absolute errors of the estimated outputs for all considered situations with complex inflow conditions, encompassing fully, partially, and overlapping waked conditions.

Scenario	Turbine	Condition	Avg. estimation error [%]	
			M_{TB} DELs	$M_{B-15\%}$ DELs
No wake steering	WT2	Fully waked	13.0	14.2
	WT3	Fully waked	10.1	13.4
Wake steering	WT1	Misaligned	16.1	13.4
	WT2	Partially waked	15.5	16.7
	WT3	Overlapping wakes	10.5	15.7
Average estimation error over all complex inflow conditions			13.0	14.7

~~For a deeper insight into~~ To further interpret these results, Fig. 7a~~and 7c show the amplitude of the Fast Fourier Transform (FFT) –~~d show the normalized FFT amplitudes of the tower-base bending ~~and~~ moment and the blade bending moment at

15% ~~blade span , respectively,~~ span for a single turbine in clean inflow ~~condition at a wind speed of 9 $\mathrm{m\,s^{-1}}$ and TI equal to 6%, while Fig. 7b and 7d show the same~~ and for WT2 in partially waked ~~condition, with an observed average wind speed of 9 $\mathrm{m\,s^{-1}}$. The OpenFAST ground-truth measurements are shown with dashed bluelines, while the estimates are represented by solid yellowlines. All FFT amplitudes are normalized relative to the peak amplitude recorded by OpenFAST.~~

conditions. OpenFAST measurements (dashed blue) are compared with digital shadow estimates (solid yellow). The digital shadow ~~is capable of capturing reasonably well the overall trend of the spectrum as the turbine moves from an aligned to a misaligned condition for the frequencies clustered around the 1 to the~~ reproduces the main spectral features, particularly around the 1P–3P ~~harmonics. The peaks of the OpenFAST-measured tower-base and blade bending moments are approximately~~ harmonics, and captures the increase in load amplitudes from aligned to waked inflow. Under waked conditions, OpenFAST peak amplitudes rise by factors of about 5 (tower) and 3 ~~times higher under waked conditions compared to the no wake condition. The errors in the peak amplitude of the tower-base bending moment~~ (blade). The digital shadow errors in peak amplitude are 14% ~~under cleaninflow conditions~~ (clean) and 46% ~~under wakedconditions. Similarly, the errors in the peak amplitude of the blade bending momentare~~ (waked) for the tower-base moment, and 18% ~~for the cleaninflow case~~ (clean) and 34% ~~for the waked condition~~(waked) for the blade moment.

Although the proposed digital shadow is clearly not providing an exact representation of the turbine behavior, the accuracy of the blade response in complex partially-waked and misaligned conditions is only slightly worse than the tower response provided by recent simpler digital shadows (Branlard et al., 2020b, 2024b), which would not be applicable in such non-symmetric conditions.

3.2 Validation against field measurements

Next, the digital shadow is ~~tested in~~ evaluated under real-world conditions ~~, using measurements obtained on~~ using measurements from a 3.5 MW eno wind turbine (eno energy GmbH). ~~The available measurements~~ Available signals include generator torque, rotor ~~rotational~~ speed, pitch angle, tower-top ~~accelerations in both FAand SS directions, and blade root bending moments in the~~ FA/SS accelerations, and blade-root flapwise and edgewise ~~directions. Additional strain gauges measure~~ bending moments, as well as strain-gauge measurements of two components of the tower-base ~~bending~~ moment and of the blade ~~bending~~ moment at 25% ~~blade~~ span. All ~~measurements~~ data are sampled at ~~a rate of~~ 10 Hz. ~~We leverage these measurements for a dual purpose: in a first step, they are used~~ These measurements serve two purposes: (i) to assess the prediction quality of the ~~predictions of the digital shadow , as discussed in~~ digital shadow (Sect. 3.2.2~~; in a second step, they are used~~); and (ii) to train a data-driven correction of the ~~corresponding~~ output model using Eq. (11) ~~, as discussed later in~~ (Sect. 3.2.4.

~~Following the same approach described in~~). Following the procedure of Sect. 2.1, the filter-internal model is ~~obtained~~ built by linearizing an existing OpenFAST model of the ~~wind turbine across a predetermined~~ turbine over a range of operating ~~conditions~~ points from cut-in to cut-out.

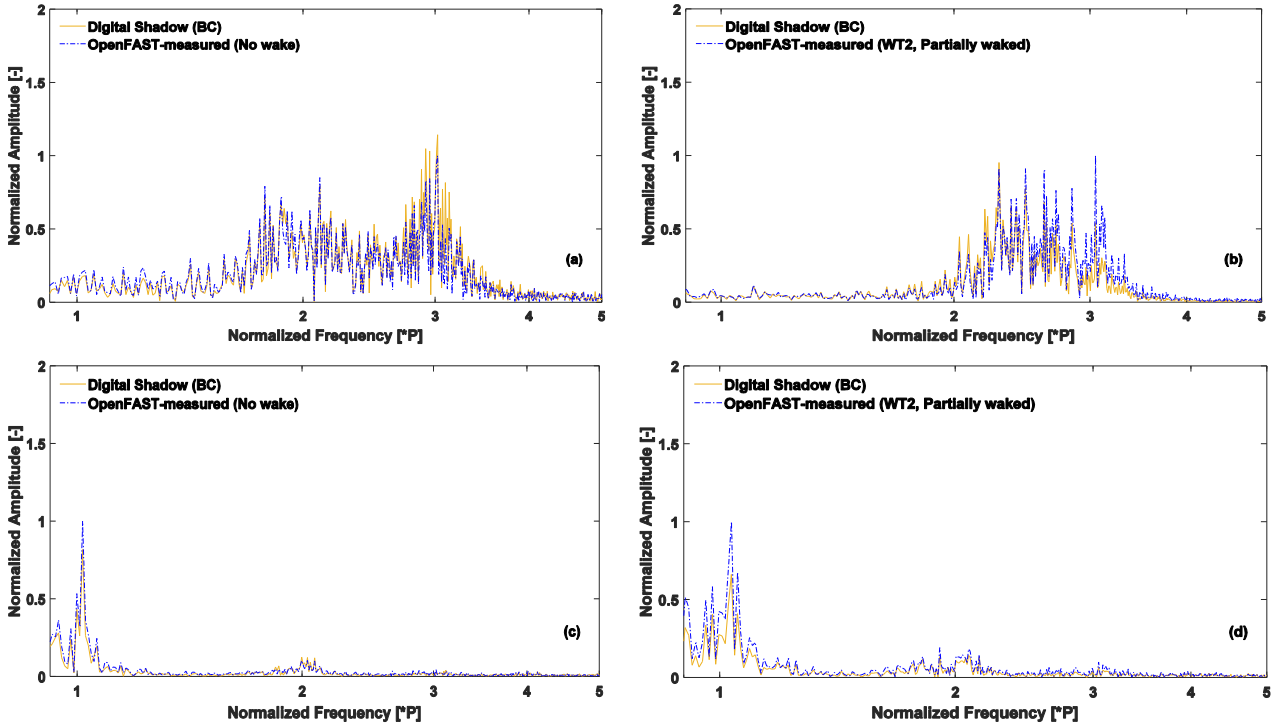

Figure 7. Spectra of the tower base bending moment (**a, b**) and the blade bending moment at 15% blade span (**c, d**) under clean inflow and partially waked conditions, respectively. The results are shown as measured on the OpenFAST model (dashed blue line) and as estimated by the digital shadow using BC (solid yellow line). The frequencies are normalized by the mean rotor speed, and all FFT amplitudes are scaled relative to the peak amplitude recorded by OpenFAST.

3.2.1 Test site

The dataset used in ~~the current~~ this study was collected at a test site ~~from 15 to 30~~ during two periods (15–30 October 2020 ~~, and 23 to 26~~ and 23–26 February 2021~~within the scope of a different project unrelated to the research described here. Measurements were used without applying any calibrations or adjustments and were filtered to eliminate~~) as part of an unrelated project. The measurements were used as recorded, without calibration or post-processing, and filtered only to remove gaps, stops, faults, ~~or any other condition that does not represent a normal power production operating mode~~and other non-power-production conditions.

The test site, illustrated in Fig. 8, is located in northeast Germany, near the village of Kirch Mulsow, in the Rostock district of Mecklenburg-Vorpommern, a few kilometers from the Baltic Sea. The terrain comprises gentle hills, open fields, and forests. Four turbines, manufactured by eno energy GmbH (eno energy GmbH), are installed at the site. The digital shadow was applied to replicate the response of WT3. The main technical specifications of WT3 and WT4 are summarized in Table 4; WT1 and WT2 are not described further, as they played no role in the present experiment.

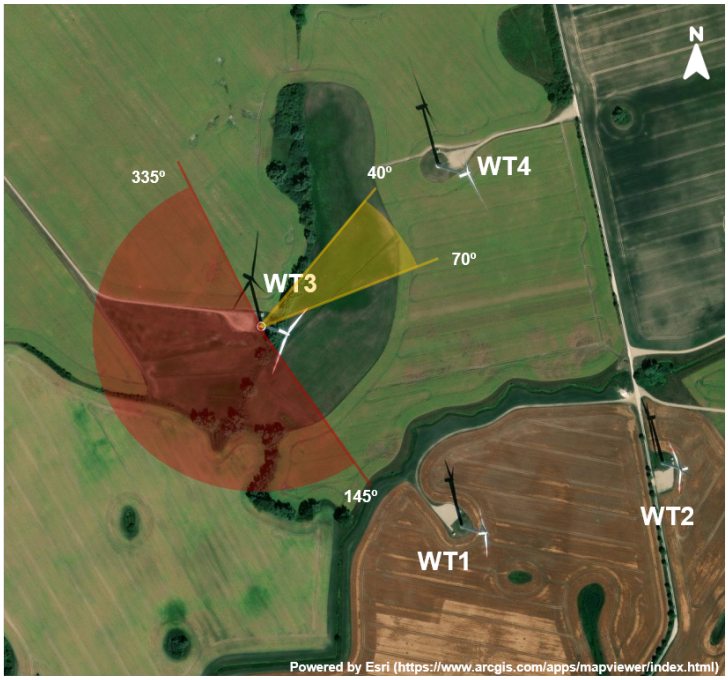

Figure 8. Layout of the test site, showing the turbine locations. The digital shadow is tested for the response of WT3. The sectors highlighted in red and yellow indicate the wind direction range during the testing period, which are characterized by clean freestream and waked conditions, respectively.

The testing period ~~is classified~~ was categorized into different inflow conditions, as ~~presented~~ summarized in Table 3. After filtering ~~to remove gaps and non-power production conditions, approximately 49 h of data were selected from the available measurement streams during the testing period under~~ out gaps and non–power-production periods, approximately 49 h of clean free-stream ~~conditions. The resulting dataset was divided~~ data were retained. This dataset was split into two subsets: the first ~~,~~ ~~comprising 38 h (approximately~~ 38 h (about 77 %~~of the total) , was~~) were used to train the correction approaches described in Sect. 2.4~~. The remaining 11 h were reserved for validation , representing a sample day with clean inflowconditions. In addition, as shown~~ , while the remaining 11 h were kept for validation and correspond to one representative day of clean inflow.

Furthermore, as indicated in Table 3, data from selected days with complex inflow ~~conditions~~ were used to ~~further assess the performance of the~~ evaluate the digital shadow under ~~complex inflow scenarios. It should be noted that~~ more challenging conditions. Importantly, no data from complex inflow ~~conditions were used for~~ scenarios were used in tuning the correction terms ~~discussed~~ presented in Sect. 2.4.1.

Wind speed and shear estimators for these turbines were developed and validated in previous studies (Schreiber et al., 2020a; Bertelè et al., 2021).

Table 3. Inflow conditions during the testing period.

Inflow conditions	Specific conditions	Wind direction [°]	Time period	Total hours	Data split [hrs]
Clean freestream	Normal	145–335	17-31 Oct. 2020	49	38 (training) / 11 (testing)
Complex inflow	Extreme vertical shear	145–335	26 Oct. 2020	3	3 (testing)
	Wake steering via yaw control	200–230	23 Feb. 2021	2.5	2.5 (testing)
	Waked	40–70	15 Oct. 2020	2	2 (testing)

Table 4. Technical specifications of the WT3 and WT4 turbines at the test site.

Wind turbine	Turbine specifications				
	Turbine model	Rotor diameter [m]	Hub height [m]	Rated power [MW]	Cut-in, rated, cut-out speeds [$\mathrm{m\,s^{-1}}$]
WT3	eno126	126	117	3.5	3.0, 12.5, 25.0
WT4	eno126	126	137	3.5	3.0, 12.5, 25.0

3.2.2 Digital shadow performance without correction

First, we assess the ability of the digital shadow ~~in estimating~~ to estimate quantities of interest ~~(in this case, loads), where~~ when no physical sensors are available. To this ~~purpose~~end, the digital shadow is fed with SCADA data, blade root load measurements, and the inflow quantities produced by the wind observers, but not with the tower-base and 25%-span blade measurements. ~~Rather, these measurements are used to assess~~ These withheld measurements are instead used to evaluate the quality of the ~~estimates of the same quantities provided by the digital shadow~~corresponding estimates.

Figure 9a and 9b ~~report the time histories of the~~ show the normalized measured (dashed blue line) and estimated (solid red line) tower-base bending moment resultant and blade bending moment resultant at 25% blade span, respectively, ~~for 11 h~~ over 11 h on a sample day (20 October 2020) ~~in the available dataset~~ under clean freestream conditions~~. On this day, the turbine experienced clean inflow conditions with~~ , characterized by an average TI of 13.5% ~~, as measured by the met mast.~~

~~Upon closer inspection of the zoomed-in insets of Fig. 9, it appears~~ (met mast). The zoomed insets reveal that the digital shadow ~~is able to follow remarkably well both the high and low-frequency variations of the measurements. However, the estimated response also exhibits~~ captures both low- and high-frequency variations well, although a clear offset ~~. This is the effect of the approximate nature of the aeroelastic model, which creates a larger~~ is present due to the plant/internal-model mismatch ~~in real-world conditions than in the simulated case analyzed in~~ between the real turbine and the approximate aeroelastic model –an effect not observed in the simulated study of Sect. 3.1.4, where ~~an identical OpenFAST model was used for defining the~~ the same OpenFAST model served as both plant and filter-internal ~~model but also served as plant~~model.

~~The~~ For this sample day, the average absolute errors are 5.9% for the tower-base ~~and~~ bending moment resultant and 21.3% for the 25%-span blade bending moment ~~resultants are found to be 5.9% and 21.3%, respectively, for the sample day shown~~

~~in Fig. 9. Additionally, considering the~~ resultant. Over the full training dataset, the ~~average absolute error for the~~ tower-base ~~bending moment resultant is~~ error averages 12.4% (~~with a minimum of~~ min: 9.7%~~and a maximum of~~ , max: 19.7%), while ~~for~~ the 25%-span blade ~~bending moment resultant is equal to 18.7% (ranging between~~ error averages 18.7% (range: 13.7%~~and~~ –23.7%).

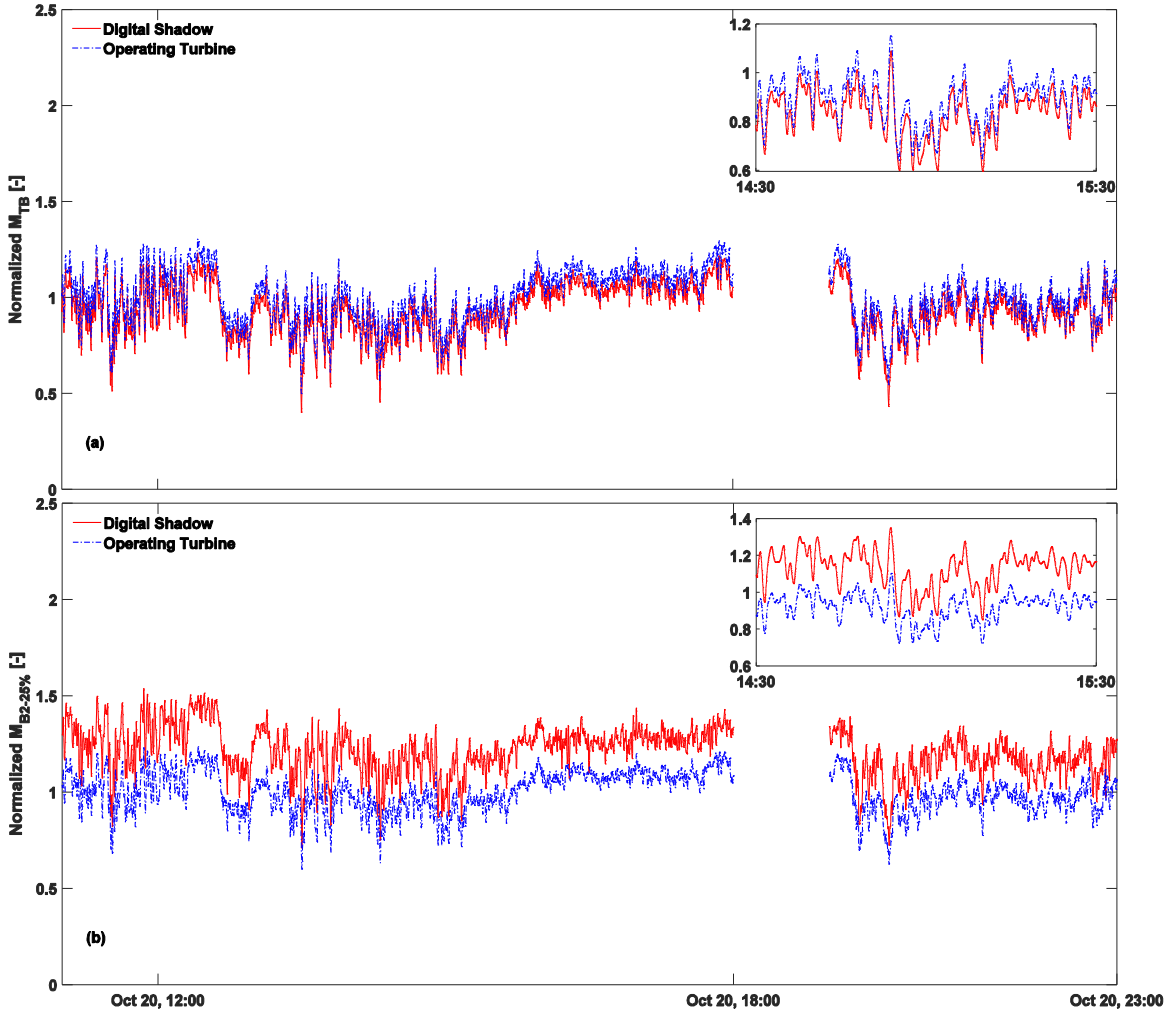

Figure 9. Time histories of tower-base bending moment **(a)** and blade bending moment at 25% blade span **(b)**, as measured (dashed blue line) and estimated by the digital shadow (solid red line) for 11 h on a sample day (20 October 2020) in the available dataset under clean freestream conditions. All values have been normalized using the same factor to preserve the confidentiality of the turbine data.

3.2.3 Virtual sensing (bias correction)

Second, ~~in order~~ to remove the observed offset, the correction of both outputs and states is ~~obtained with~~ performed using the BC approach described in Sect. 2.4.1 and based on Eqs. (10).

~~The empirical~~ The tuning of the correction terms ~~was guided by the quality of the measurements at the tower top and blade root, utilizing the data streams available~~ followed the procedure of Sect. 3.1.3, relying on tower-top and blade-root measurements collected during the testing period~~, as described in Sect. 3.1.3.~~.

First, the static force term $\mathbf{f}_0$ was ~~modified by trial and error~~ adjusted through an iterative tuning process until no further improvement was ~~possible. It was found that this term depends primarily~~ obtained. This term was found to depend mainly on wind speed, ~~while the other terms of the scheduling set~~ whereas the other scheduling variables $\mathbf{s}$ had ~~only a negligible effect for the data streams~~ negligible influence under clean freestream conditions. While a manual tuning strategy was adopted in this work, more systematic or automated optimization approaches (e.g., gradient-based, Bayesian, or heuristic methods (Nocedal and Wright, 2006)) could be employed and represent a promising direction for future development. Next, the bias term $\mathbf{b}$ was activated, and its driving process noise was ~~calibrated~~ tuned to further reduce ~~the error in the measurements. As for~~ measurement errors. As with the process noise affecting the dynamic equilibrium equations, ~~this calibration term again did not exhibit a~~ no significant dependency on wind speed or turbulence intensity ~~. It should be noted that, considering the training dataset, after~~ was observed. After tuning, the average absolute ~~error~~ errors over the training dataset were 3.1% for the tower-top acceleration resultant ~~is 3.1%, while it is~~ and 3.5% for the ~~blade root~~ blade-root bending moment resultant.

Table 5 ~~presents an overview of~~ summarizes the average absolute errors and ~~the estimated~~ output DELs for the ~~complete dataset, categorized~~ full dataset, grouped by the inflow ~~conditions~~ classes defined in Table 3.

~~After implementing the bias correction,~~ For the same sample day shown in Fig. 10, the bias correction reduces the average absolute errors for M_{TB} and $M_{B-25\%}$ ~~decreased~~ to 4.2% and 2.7%, respectively, ~~for the same sample day shown in Fig. 10,~~ indicating that the offset ~~in the estimations~~ has been effectively removed. ~~In addition, the~~ The corresponding DEL estimation errors are 4.3% for M_{TB} and ~~$M_{B-25\%}$ became 4.3% and~~ 9.1% ~~, respectively~~for $M_{B-25\%}$. Overall, the BC approach ~~seems to be capable of tracking~~ accurately tracks both low- and high-frequency fluctuations~~in the quantities of interest, and of providing accurate estimates of their DELs~~, providing reliable DEL estimates for the quantities of interest.

It ~~should be mentioned~~ is worth noting that the BC method ~~appears to be~~ proves more effective in ~~correcting estimated quantities in the real field case~~ the field than in the simulation environment. This ~~could be due to several reasons, such as~~ may stem from the higher TI and ~~a sampling rate that is ten times faster in the simulation case. In fact, the higher sampling rate introduces more~~ the tenfold faster sampling rate used in simulations, which introduces additional high-frequency fluctuations ~~, which are more challenging~~ that are harder to estimate accurately.

~~Since the bias correction approach is a generalizable method and has demonstrated strong performance, the~~ Given the strong and generalizable performance of the BC approach, all remaining results for complex inflow conditions are obtained using this ~~approach. This decision is further motivated by one of the key applications~~ method. This choice also aligns with a key application of the digital shadow ~~, which acts~~ as a virtual sensor ~~to estimate~~ for quantities that cannot be ~~measured directly~~

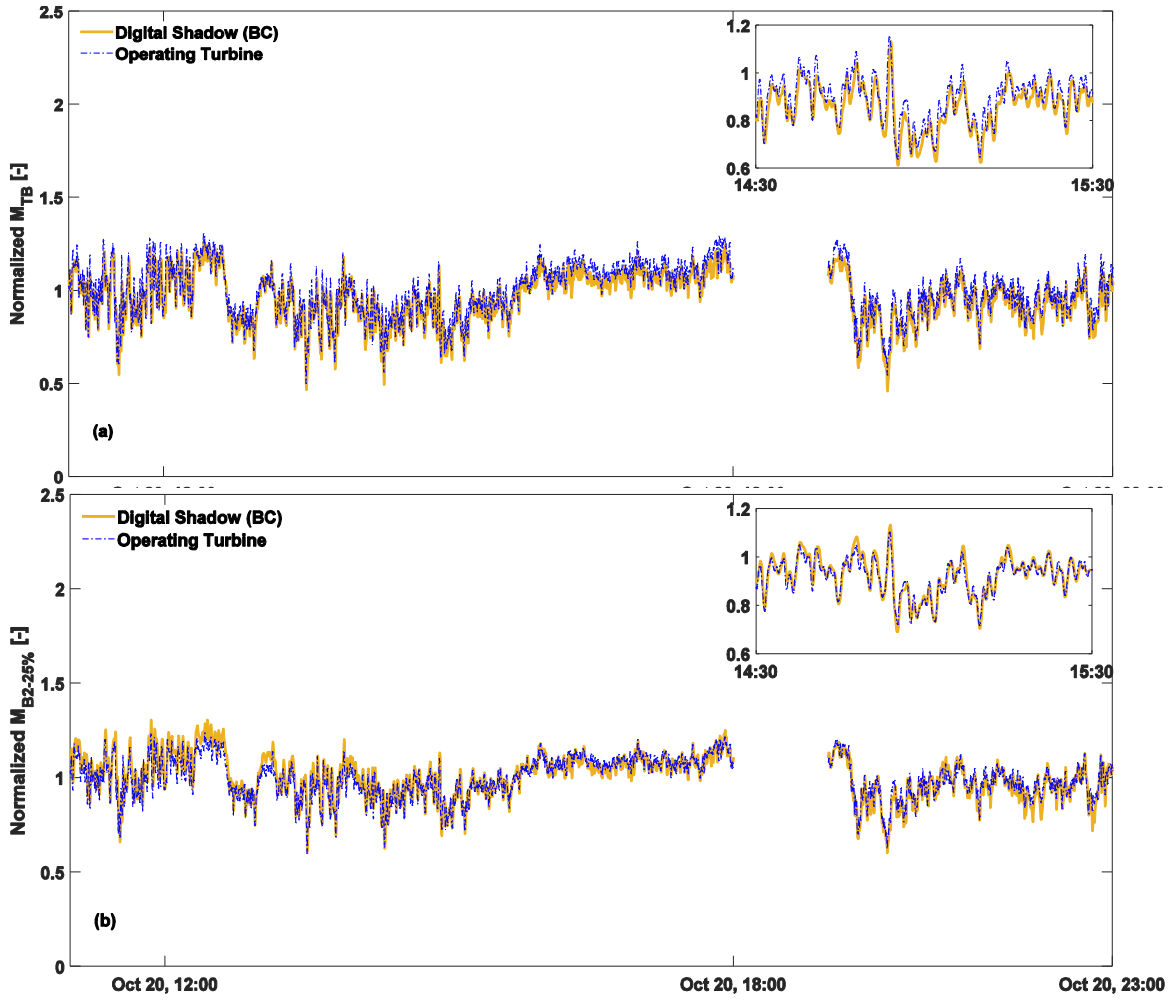

Figure 10. Time histories of the tower-base bending moment **(a)** and blade bending moment at 25% blade span **(b)** for 11 h on a sample day (20 October 2020) in the available dataset under clean freestream conditions. Measurements: dashed blue line; corrected estimates of the digital shadow using BC: solid yellow line. All values have been normalized using the same factor to preserve the confidentiality of the measured turbine data.

~~due to~~ directly measured for technical or economic ~~limitations. To illustrate these results, time history plots are provided~~ reasons. For brevity, time-history plots are shown only for the waked inflow ~~conditions~~ case (Fig. 11), as this scenario is particularly ~~relevant and informative for understanding~~ informative regarding model behavior under complex aerodynamic interactions. Figures for ~~other inflow conditions are omitted to maintain conciseness and avoid redundancy~~the other inflow classes are omitted for conciseness.

– ***Extreme vertical shear:***

The ~~bias correction – tuned using~~ BC correction –tuned exclusively on the training dataset defined in Table 3– was developed without using any ~~data from complex inflow conditions. Despite this~~complex-inflow data. Even so, the average absolute errors for M_{TB} and $M_{B-25\%}$ are 6.0% and 2.4%, respectively, for the ~~dataset corresponding to the~~ extreme vertical shear ~~scenario defined in Table 3. Additionally, the~~ dataset. The corresponding DEL estimation errors ~~for M_{TB} and $M_{B-25\%}$~~ are 6.7% and 7.3%~~, respectively, demonstrating the ability of the BC approach to provide estimations with~~ . These results confirm that the BC approach maintains errors below 10% ~~, even under extreme shear conditions. It should be noted that~~ even under severe shear conditions, where the power law ~~vertical shear~~ exponent ranges from 0.15 to 0.72 ~~, with an average value of~~ (average 0.42).

– ***Wake steering via yaw control:***

For the ~~dataset corresponding to the wake steering via yaw control scenariodefined in Table 3~~wake-steering scenario, the average absolute errors for M_{TB} and $M_{B-25\%}$ are 6.2% and 2.3%, respectively~~. Additionally,~~ , while the DEL estimation errors ~~for M_{TB} and $M_{B-25\%}$~~ are 0.9% and 8.0%~~, respectively, with yaw misalignment ranging from~~ . Yaw misalignment varies between $-16°$ ~~to~~ and $11°$. ~~It is important to note that the turbine dynamics in wake steering control mode are~~ Despite the inherently more complex ~~, further highlighting the performance of the digital shadow under complex inflow~~ dynamics associated with wake steering, the digital shadow continues to perform robustly under these conditions.

– ***Waked:***

Figures 11(a) ~~,~~through 11(~~b), 11(c), and 11(d) present the time histories of the~~ d) show the tower-base bending moment, the 25%-span blade bending moment ~~resultants, and~~ resultant, and the vertical and horizontal shears ~~, respectively, for the dataset corresponding to the waked scenario defined in Table 3~~for the waked dataset. Measurements are ~~indicated by a dashed blue line, while the fine-tuned~~ shown as dashed blue lines, and BC-corrected ~~values are shown with a solid yellow line. As illustrated in Fig. 11(c), the~~ estimates as solid yellow lines. The power law vertical shear has an average value of -0.15 ~~, marked by a~~ (dark red dashed line~~. This condition is~~), attributed to the higher hub height of WT4 and ~~the influence of its wake~~ its wake influence on WT3. ~~Furthermore, as shown in Fig. 11(d), the horizontal shear – indicated by a~~ The horizontal shear averages -0.12 (light red dashed line~~ – has an average value of -0.12~~), further confirming ~~the presence of waked conditionson WT3~~strongly waked conditions.

~~The~~ For this dataset, the average absolute errors for M_{TB} and $M_{B-25\%}$ are 11.4% and 5.1%, respectively, while the DEL estimation errors are 0.9% and 13.3%~~, respectively, for the dataset presented in Fig. 11. These results indicate that, while~~ . Although the BC approach generally performs well, the ~~inherently~~ complex turbine dynamics and ~~the significant~~ large variations in vertical and horizontal shear under wake conditions ~~contribute to the observed discrepancies, resulting in errors slightly~~ result in slightly higher errors, with some values exceeding 10%.

Overall, the range of average estimation errors is consistent with the findings of previous studies (Abdallah et al., 2017; Branlard et al., 2020a, b, 2024a), which ~~, however, used a reduced number of degrees of freedom (DOFs), did not account for~~ relied on fewer DOFs, neglected blade dynamics, and were not validated under complex inflow~~conditions~~.

However While the digital shadow remains effective under all tested conditions, the slightly higher estimation errors observed under complex inflow conditions suggest that , while the model is effective, further refinement using errors in complex inflow indicate that further refinement could be achieved with a larger dataset may be necessary to reduce residual offsets and achieve more accurate predictions in such scenarios. Additionally. In particular, the tuning of the BC correction term could be enhanced by incorporating not only wind speed but also terms may benefit from explicitly incorporating variations in vertical and horizontal shear, as well as yaw misalignment, in addition to wind speed.

Table 5. Overview of average absolute errors and estimated output damage equivalent loads (DELs) under various inflow conditions.

Inflow conditions	Time duration [hrs]	Estimation error [%]			
		M_{TB} Avg. Abs.	$M_{B-25\%}$ Avg. Abs.	M_{TB} DELs	$M_{B-25\%}$ DELs
Clean freestream	11	4.2	2.7	4.3	9.1
Extreme vertical shear	3	6.0	2.4	6.7	7.3
Wake steering via yaw control	2.5	6.2	2.3	0.9	8.0
Waked	2	11.4	5.1	0.9	13.3

3.2.4 Condition monitoring

Next, the measurements of the tower-base and 25%-span blade bending moments were utilized used to implement and validate a data-driven a posteriori error *a posteriori* correction of the corresponding output equations, following Eq. (11), in order to provide a to obtain high-quality prediction predictions of these quantities. In this second scenarioconfiguration, the turbine is permanently equipped with sensorsinstrumented, and the digital shadow provides expected values for these quantities of interest based on the current operational under the current operating conditions. A CM activity (not discussed or analyzed further in this work) can then be based on the comparison of measurements and predictions , thereby detecting possible anomalies. The quality of the predictions is quantified in terms of further discussed here) may then compare predictions and measurements to detect anomalies. Prediction quality is quantified using the Root Mean Squared Percentage Error (RMSPE), which is commonly used commonly adopted in CM (Liu et al., 2023).

The same dataset presented used in Sect. 3.2.2 was used for training, with the sample day allocated employed, with a sample day reserved for validation. The NN-based correction term was implemented using the MATLAB Deep Learning Toolbox (The MathWorks, Inc., 2022)was used to implement and train the NN-based correction term. Following a . A basic trial-and-error approach, study led to a neural network architecture with a single hidden layer containing with one hidden layer of 16 neuronswas selected. During training, the Polak-Ribiére Conjugate Gradient algorithm (traincgp) and BFGS quasi-Newton backpropagation (trainbfg) yielded the best performance for the tower-base and 25%-span blade bending moment, respectively. Notably, the achieved RMSPEs for the training of the The resulting RMSPEs during training were approximately 0.8% for the tower-base and 0.9% for the 25%-span blade bending moments were as low as about 0.8% and 0.9%, respectivelymoment.

Figures 12(a) and 12(b) report time histories of the tower-base and 25%-span blade bending moment resultants, respectively. Measurements are shown with a dashed blue line and the corrected ~~ones~~ estimates with a solid green line. Before implementing the ~~a-posteriori~~ *a posteriori* error correction, the RMSPE for M_{TB} and $M_{B-25\%}$ were 6.1% and 21.6%, respectively. After data-driven correction, these values dropped to 1.3% and 1.5%, respectively.

A closer inspection of the time series also shows that the NN-corrected model captures most of the short-term intermittency present in the measured loads, including the majority of fast fluctuations driven by turbulent inflow. The sharpest intermittent spikes observed in real turbine data are only partially reproduced, reflecting the inherent smoothing of the underlying linear model. Nevertheless, the dominant variability and overall intermittency level are matched well enough for the CM application considered here. Overall, it appears that the proposed data-driven approach is ~~very effective at~~ highly effective in correcting the output equations, as both slow and fast fluctuations of the two quantities of interest are ~~followed~~ tracked with remarkable accuracy, although it cannot improve the state model.

4 Conclusions

We have presented, verified, and validated ~~with respect to one field dataset a wind turbine digital shadow~~ a digital shadow of a wind turbine, first in a simulation environment under freestream, waked, and wake-steering scenarios, and then against a field dataset. Building on a classical Kalman filtering ~~approach, the proposed digital shadow formulation~~ framework, the approach linearizes an existing and trusted aeroservoelastic model to derive the filter-internal linear model. Reusing ~~existing~~ such models reduces development time, leverages ~~resources already invested in~~ prior tuning and validation efforts, increases confidence in ~~the~~ results, and avoids duplication of ~~effort~~work.

~~However, departing from the existing literature, we have included in the model the~~ Departing from existing studies, tower side-side and ~~the~~ rotor blade DOFs ~~in order~~ were included to support more general operating conditions, such as ~~the ones deriving from sheared inflows, waked , and yaw-misaligned operations~~sheared inflow, waked flow, and yaw misalignment. Since the linearization must now span a ~~much wider solution spacethan in existing similar approaches~~broader solution space, the filter-internal model is scheduled with respect to ~~a number of parameters tasked with~~ parameters representing the main drivers of the turbine response. ~~The rotor as a sensor technology is used to estimate these scheduling parameters~~ These scheduling parameters are estimated in real time ~~during operation~~ using the rotor as a sensor technology from SCADA and blade load measurements.

~~Testing in a simulation environment showed that the accuracy of the states of the digital shadow generally remains~~ Simulation testing showed state-estimation errors generally below 10% across all ~~tested conditions. The average absolute error for DELs is in the range of~~ conditions. DEL errors ranged from 5%–15%, ~~the larger values being observed in higher ambient turbulence and in waked conditions~~with higher values under elevated turbulence and waked inflow, as expected. Slightly larger errors (~~16.1%) were observed for a misaligned turbine, where the complex behavior of the rotor is probably not completely captured by the~~ 16.1%) occurred under yaw misalignment, reflecting limits of the linearized model. ~~Remarkably, the accuracy of the digital shadow applied to a field dataset was very similar to the one obtained in the simulationenvironment~~Field results were

remarkably similar to those in simulation, even without ~~any~~ ad hoc tuning~~of the model. However, clear biases were present, which are indicative of the limits of the~~ , although clear biases indicated limitations of the underlying filter-internal model.

~~Indeed, the main weakness~~ A key limitation of a digital shadow is its ~~reliance~~ dependence on a white state-space model~~. This is invariably affected by errors, which in turn will always limit the quality of the estimates that it can produce. To cope with thisissue, we have investigated two alternative ways of augmenting the model with~~ , which is inevitably affected by modelling errors. To address this, two alternative data-driven correction ~~terms, resulting in grey models of greatly improved predictive~~ strategies were examined, yielding grey models with substantially improved prediction accuracy.

~~In particular, the fine-tuned BC approach demonstrated robust performance~~ The BC approach performed robustly under complex inflow conditions, including extreme vertical shear, waked flow, and wake-steering control~~, during field validation. Despite these challenging scenarios, the errors remained small across all tested cases, further highlighting the~~ . Errors remained small in all cases, demonstrating strong reliability and adaptability~~of the proposed approach.~~

~~The bias correction method demonstrated strong performance, lowering the average absolute error from approximately~~ . Overall, the BC method reduced average absolute errors from roughly 20% to ~~a range of~~ 2%–11%~~. Additionally, the average DEL estimation error was reduced to between~~ , and DEL estimation errors to 1%–13%~~. These improvements represent a substantial advancement over results reported in the~~ , representing a significant improvement over recent literature and ~~highlight the potential of the proposed approach~~ underscoring its potential for fatigue analysis, lifetime ~~consumption~~ estimation, and load-aware control~~strategies~~. In parallel, the ~~neural correction of the selected outputs of interest also~~ NN-based a posteriori output correction proved highly effective, reducing ~~the~~ load RMSPE from ~~a range of~~ 10%–15% to ~~approximately~~ about 1%~~. This outcome~~ , which is particularly promising for ~~the application of the digital shadow in CM scenarios~~CM applications.

~~The approach discussed here can be improved in several ways. For example, other~~ Several improvements are possible. Additional inflow quantities may ~~be necessary to further improve the~~ further enhance scheduling of the filter-internal model~~. One such parameter is veer, which, however, could be readily added to the scheduling parameters, as it can be estimated with the~~ ; for instance, veer could be included and estimated using rotor as a sensor technology by ~~expanding the load harmonics to include the~~ extending the harmonic content to 2P ~~(?). Regarding validation, while the current results are encouraging, it is clear that the proposed approach should be tested on~~ (Bertelè et al., 2024). Validation should also be expanded to larger field datasets covering ~~a wider range of~~ broader inflow and operating conditions, as well as different turbine types. ~~In addition~~Moreover, the tuning of the BC correction term could be ~~improved by considering not only wind speed but also~~ refined by accounting for variations in vertical and horizontal shear~~and~~ , as well as yaw misalignment, which ~~also~~ would require more extensive data. We also note that the wind speed and shear observers smooth some high-frequency content; however, since these quantities are used solely for model scheduling, this limitation has limited practical impact.

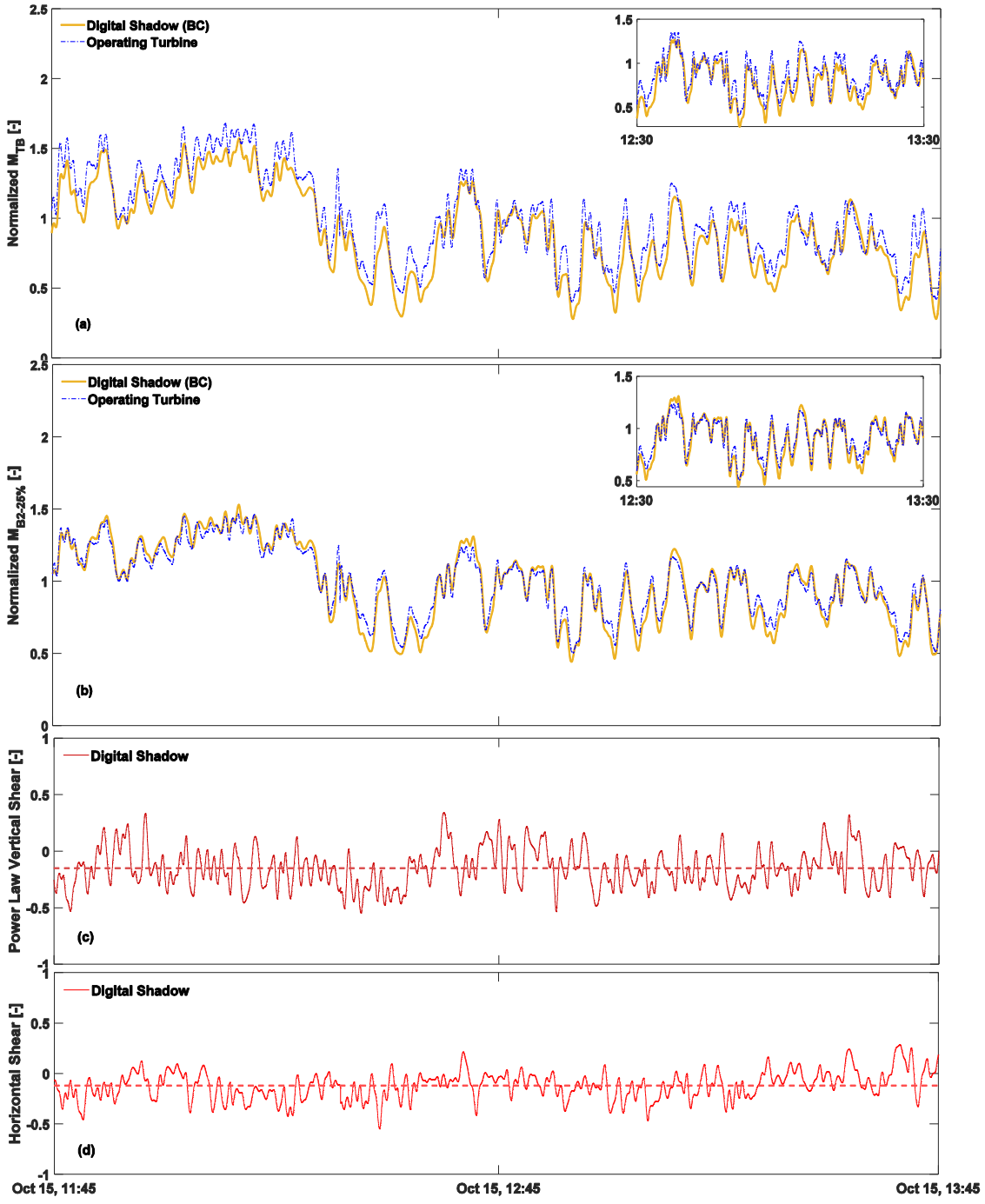

Figure 11. Time histories of the tower-base bending moment **(a)**, blade bending moment at 25% blade span **(b)**, vertical shear **(c)**, and horizontal shears **(d)**. Measurements: dashed blue line; corrected estimates of the digital shadow using ~~fine-tuned~~ BC: solid yellow line. The shears are shown with solid red lines, with an average value marked by red dashed lines. All values have been normalized using the same factor to preserve the confidentiality of the measured turbine data.

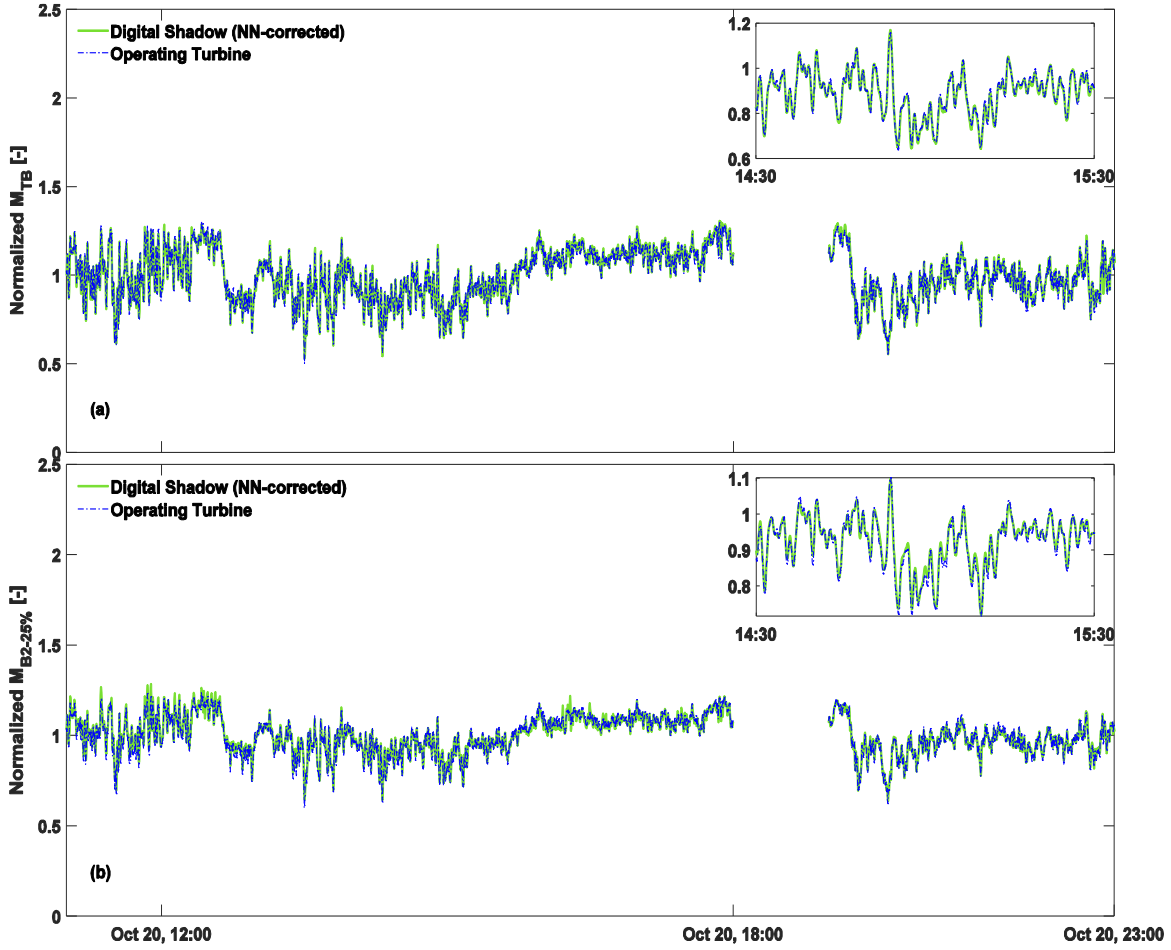

Figure 12. Time histories of the tower-base bending moment **(a)** and blade bending moment at 25% blade span **(b)**. Measurements: dashed blue line; corrected estimates of the digital shadow using NN: solid green line. All values have been normalized using the same factor to preserve the confidentiality of the measured turbine data.

Appendix A: Nomenclature

$\mathbf{b}$	Vector of sensor biases
$\mathbf{f}_0$	Static correction force
$\mathbf{i}$	Input vector of the inflow estimator
$\mathbf{p}$	Vector of free network parameters
$\mathbf{q}$	Vector of generalized displacements
$\mathbf{s}$	Vector of scheduling parameters
$\mathbf{u}$	Input vector
$\mathbf{v}$	Vector of generalized velocities
$\mathbf{y}$	Vector of outputs for Kalman innovation
$\mathbf{z}$	Vector of other outputs of interest
ν	Measurement noise vector
ω	Process noise vector
A	Rotor swept area
c	Generic output of the wind inflow characteristic observer
C_p	Power coefficient
d	Displacement
J	Rotor inertia
κ_h	Horizontal shear
M	Bending moment resultant
m	Bending moment component
Q	Torque
R	Rotor radius
V	Wind speed
α	Vertical power-law shear exponent
γ	Misalignment angle
ϵ	Output correction term
θ	Blade pitch angle
λ	Tip speed ratio
ρ	Air density
ψ	Rotor azimuthal position

Ω	Rotor rotational speed
$(\cdot)^E$	Edgewise component
$(\cdot)^F$	Flapwise component
$(\cdot)^{FA}$	Fore-aft component
$(\cdot)^{SS}$	Side-side component
$(\cdot)^{IP}$	In-plane component
$(\cdot)^{OP}$	Out-of-plane component
$(\cdot)^{NN}$	Quantity corrected by a neural network
$(\cdot)_{1c}$	1P cosine component
$(\cdot)_{1s}$	1P sine component
$(\cdot)_{Bi}$	Quantity referred to the ith blade
$(\cdot)_{B-s\%}$	Quantity referred to the $s\%$ spanwise location
$(\cdot)_{TB}$	Quantity referred to the base of the tower
$(\cdot)_E$	Estimated quantity
$(\cdot)_M$	Measured quantity
$(\cdot)_0$	Reference equilibrium condition
$\delta(\cdot)$	Perturbation about a reference equilibrium condition
BEM	Blade element momentum
CFD	Computational fluid dynamics
CM	Condition monitoring
DEL	Damage-equivalent load
DOF	Degree of freedom
FA	Fore-aft
FEM	Finite element method
FFT	Fast Fourier transform
LUT	Look-up table
NN	Neural network
BC	Bias correction
PSD	Power spectral density
RMSPE	Root mean squared percentage error
ROM	Reduced order model
RWT	~Reference wind turbine
SCADA	Supervisory control and data acquisition

SS	Side-side
TI	Turbulence intensity
WT	Wind turbine

Data availability. All figures and the data used to generate them can be retrieved in Pickle Python and MATLAB formats via https://doi.org/10.5281/zenodo.11519470. The field dataset is the property of eno energy systems GmbH.

Author contributions. CLB developed the core idea of the research and supervised the work. HH implemented the digital shadow, performed the numerical simulations, and processed the field dataset. Both authors contributed equally to the interpretation of the results and to the writing of the paper.

Competing interests. At least one of the (co-)authors is a member of the editorial board of *Wind Energy Science*.

Acknowledgements. The technical assistance from Marta Bertelè, Carlo. L Sucameli, Adrien Guilloré, and Abhinav Anand is acknowledged and greatly appreciated. The authors express their gratitude to eno energy systems GmbH, which granted access to the turbine aeroelastic model and to the field dataset.

Financial support. This work has been supported in part by the PowerTracker (FKZ: 03EE2036A), CompactWind II project (FKZ: 0325492G), and Life-Odometer (FKZ: 03EE3037B) projects, which receive funding from the German Federal Ministry for Economic Affairs and Climate Action (BMWK). Additional support has been provided by the MERIDIONAL project, which receives funding from the European Union's Horizon Europe program under the grant agreement no. 101084216.

References

Abdallah, I., Tatsis, K., and Chatzi, E.: Fatigue assessment of a wind turbine blade when output from multiple aero-elastic simulators are available, Procedia Engineering, 199, 3170–3175, https://doi.org/https://doi.org/10.1016/j.proeng.2017.09.509, x International Conference on Structural Dynamics, EURODYN 2017, 2017.

Anand, A. and Bottasso, C. L.: Reducing Plant-Model Mismatch for Economic Model Predictive Control of Wind Turbine Fatigue by a Data-Driven Approach, in: 2023 American Control Conference (ACC), 979-8-3503-2806-6, pp. 1473–1479, https://doi.org/10.23919/ACC55779.2023.10156501, 2023.

Bangalore, P., Letzgus, S., Karlsson, D., and Patriksson, M.: An artificial neural network-based condition monitoring method for wind turbines, with application to the monitoring of the gearbox, Wind Energy, 20, 1421–1438, https://doi.org/https://doi.org/10.1002/we.2102, 2017.

Bernhammer, L. O., van Kuik, G. A., and De Breuker, R.: Fatigue and extreme load reduction of wind turbine components using smart rotors, Journal of Wind Engineering and Industrial Aerodynamics, 154, 84–95, https://doi.org/https://doi.org/10.1016/j.jweia.2016.04.001, 2016.

Bertelè, M., Bottasso, C. L., and Schreiber, J.: Wind inflow observation from load harmonics: initial steps towards a field validation, Wind Energy Science, 6, 759–775, https://doi.org/10.5194/wes-6-759-2021, 2021.

Bertelè, M., Meyer, P. J., Sucameli, C. R., Fricke, J., Wegner, A., Gottschall, J., and Bottasso, C. L.: The rotor as a sensor – Observing shear and veer from the operational data of a large wind turbine, Wind Energy Science, 9, 1419–1429, https://doi.org/10.5194/wes-9-1419-2024, 2024.

Boorsma, K., Greco, L., and Bedon, G.: Rotor wake engineering models for aeroelastic applications, Journal of Physics: Conference Series, 1037, 062 013, https://doi.org/10.1088/1742-6596/1037/6/062013, 2018.

Bottasso, C., Campagnolo, F., Croce, A., and Tibaldi, C.: Optimization-based study of bend–twist coupled rotor blades for passive and integrated passive/active load alleviation, Wind Energy, 16, 1149–1166, https://doi.org/https://doi.org/10.1002/we.1543, 2013.

Bottasso, C. L., Chang, C.-S., Croce, A., Leonello, D., and Riviello, L.: Adaptive planning and tracking of trajectories for the simulation of maneuvers with multibody models, Computer Methods in Applied Mechanics and Engineering, 195, 7052–7072, https://doi.org/https://doi.org/10.1016/j.cma.2005.03.011, multibody Dynamics Analysis, 2006.

Branlard, E., Giardina, D., and Brown, C. S. D.: Augmented Kalman filter with a reduced mechanical model to estimate tower loads on a land-based wind turbine: a step towards digital-twin simulations, Wind Energy Science, 5, 1155–1167, https://doi.org/10.5194/wes-5-1155-2020, 2020a.

Branlard, E., Jonkman, J., Dana, S., and Doubrawa, P.: A digital twin based on OpenFAST linearizations for real-time load and fatigue estimation of land-based turbines, Journal of Physics: Conference Series, 1618, 022 030, https://doi.org/10.1088/1742-6596/1618/2/022030, 2020b.

Branlard, E., Jonkman, J., Brown, C., and Zhang, J.: A digital twin solution for floating offshore wind turbines validated using a full-scale prototype, Wind Energy Science, 9, 1–24, https://doi.org/10.5194/wes-9-1-2024, 2024a.

Branlard, E., Jonkman, J., Lee, B., Jonkman, B., Singh, M., Mayda, E., and Dixon, K.: Improvements to the Blade Element Momentum Formulation of OpenFAST for Skewed Inflows, Journal of Physics: Conference Series, 2767, 022 003, https://doi.org/10.1088/1742-6596/2767/2/022003, 2024b.

Branlard, E. S. P.: Flexible multibody dynamics using joint coordinates and the Rayleigh-Ritz approximation: The general framework behind and beyond Flex, Wind Energy, 22, 877–893, https://doi.org/https://doi.org/10.1002/we.2327, 2019.

Burden, F. and Winkler, D.: Bayesian Regularization of Neural Networks, pp. 23–42, Humana Press, Totowa, NJ, ISBN 978-1-60327-101-1, https://doi.org/10.1007/978-1-60327-101-1_3, 2009.

Chen, J., Pan, J., Li, Z., Zi, Y., and Chen, X.: Generator bearing fault diagnosis for wind turbine via empirical wavelet transform using measured vibration signals, Renewable Energy, 89, 80–92, https://doi.org/https://doi.org/10.1016/j.renene.2015.12.010, 2016.

Chui, C. K. and Chen, G.: Kalman Filtering with Real-Time Applications, Springer, 1999.

Coleman, R. P. and Feingold, A. M.: Theory of Self-Excited Mechanical Oscillations of Helicopter Rotors with Hinged Blades, Technical Report NACA TN 1351, NACA, https://digital.library.unt.edu/ark:/67531/metadc56181/m2/1/high_res_d/19930084623.pdf, last accessed: 07 June 2024, 1958.

Dimitrov, N., Kelly, M. C., Vignaroli, A., and Berg, J.: From wind to loads: wind turbine site-specific load estimation with surrogate models trained on high-fidelity load databases, Wind Energy Science, 3, 767–790, https://doi.org/10.5194/wes-3-767-2018, 2018.

Drécourt, J.-P., Madsen, H., and Rosbjerg, D.: Bias aware Kalman filters: Comparison and improvements, Advances in Water Resources, 29, 707–718, https://doi.org/https://doi.org/10.1016/j.advwatres.2005.07.006, 2006.

eno energy GmbH: https://www.eno-energy.com/, eno energy GmbH, last access on 15.02.2024.

Evans, M., Han, T., and Shuchun, Z.: Development and validation of real time load estimator on Goldwind 6 MW wind turbine, Journal of Physics: Conference Series, 1037, 032 021, https://doi.org/10.1088/1742-6596/1037/3/032021, 2018.

Grewal, M. S. and Andrews, A. P.: Kalman Filtering: Theory and Practice with MATLAB, John Wiley & Sons, Inc., 2008.

Grewal, M. S. and Andrews, A. P.: Kalman Filtering: Theory and Practice Using Matlab, John Wiley & Sons, Inc., https://doi.org/https://doi.org/10.1002/9781118984987, 2014.

Guilloré, A., Campagnolo, F., and Bottasso, C. L.: A control-oriented load surrogate model based on sector-averaged inflow quantities: capturing damage for unwaked, waked, wake-steering and curtailed wind turbines, Journal of Physics: Conference Series, 2767, 032 019, https://doi.org/10.1088/1742-6596/2767/3/032019, 2024.

Hoghooghi, H.: Load Alleviation on Multi-Megawatt Wind Turbines Based on Measured Dynamic Response of Wind Turbine, Doctoral thesis, ETH Zurich, Zurich, https://doi.org/10.3929/ethz-b-000492802, 2021.

Hoghooghi, H., Chokani, N., and Abhari, R.: Effectiveness of individual pitch control on a 5MW downwind turbine, Renewable Energy, 139, 435–446, https://doi.org/https://doi.org/10.1016/j.renene.2019.02.088, 2019a.

Hoghooghi, H., Chokani, N., and Abhari, R. S.: Enhanced Yaw Stability of Downwind Turbines, Journal of Physics: Conference Series, 1356, 012 020, https://doi.org/10.1088/1742-6596/1356/1/012020, 2019b.

Hoghooghi, H., Chokani, N., and Abhari, R.: Optical measurements of multi-megawatt wind turbine dynamic response, Journal of Wind Engineering and Industrial Aerodynamics, 206, 104 214, https://doi.org/https://doi.org/10.1016/j.jweia.2020.104214, 2020a.

Hoghooghi, H., Chokani, N., and Abhari, R. S.: Individual Blade Pitch Control for Extended Fatigue Lifetime of Multi-Megawatt Wind Turbines, Journal of Physics: Conference Series, 1618, 022 008, https://doi.org/10.1088/1742-6596/1618/2/022008, 2020b.

Hoghooghi, H., Chokani, N., and Abhari, R. S.: A novel optimised nacelle to alleviate wind turbine unsteady loads, Journal of Wind Engineering and Industrial Aerodynamics, 219, 104 817, https://doi.org/https://doi.org/10.1016/j.jweia.2021.104817, 2021.

Hoghooghi, H., Bertelè, M., Anand, A., and Bottasso, C. L.: A wind turbine digital shadow with tower and blade degrees of freedom - Preliminary results and comparison with a simple tower fore-aft model, Journal of Physics: Conference Series, 2767, 032 026, https://doi.org/10.1088/1742-6596/2767/3/032026, 2024.

IEA3.37MW(2023): https://github.com/IEAWindTask37/IEA-3.4-130-RWT/tree/master, the onshore reference wind turbine developed within IEA Wind Task 37, last access on 01.08.2023.

IEC: IEC 61400-1 Wind turbines: Design requirements, International Electrotechnical Commision, 2005.

Iliopoulos, A., Shirzadeh, R., Weijtjens, W., Guillaume, P., Hemelrijck, D. V., and Devriendt, C.: A modal decomposition and expansion approach for prediction of dynamic responses on a monopile offshore wind turbine using a limited number of vibration sensors, Mechanical Systems and Signal Processing, 68-69, 84–104, https://doi.org/https://doi.org/10.1016/j.ymssp.2015.07.016, 2016.

Jacquelin, E., Bennani, A., and Hamelin, P.: Force reconstruction: analysis and regularization of a deconvolution problem, Journal of Sound and Vibration, 265, 81–107, https://doi.org/https://doi.org/10.1016/S0022-460X(02)01441-4, 2003.

Jonkman, J. and Shaler, K.: FAST.Farm User's Guide and Theory Manual, Tech. Rep. NREL/TP-5000-78485, National Renewable Energy Laboratory (NREL), 2021.

Jonkman, J. M., Wright, A. D., Hayman, G. J., and Robertson, A. N.: Full-System Linearization for Floating Offshore Wind Turbines in OpenFAST, ASME 2018 1st International Offshore Wind Technical Conference, V001T01A028, https://doi.org/10.1115/IOWTC2018-1025, 2018.

Kim, K.-H., Bertelè, M., and Bottasso, C. L.: Wind inflow observation from load harmonics via neural networks: A simulation and field study, Renewable Energy, 204, 300–312, https://doi.org/https://doi.org/10.1016/j.renene.2022.12.051, 2023.

Liu, J., Wang, X., Xie, F., Wu, S., and Li, D.: Condition monitoring of wind turbines with the implementation of spatio-temporal graph neural network, Engineering Applications of Artificial Intelligence, 121, 106 000, https://doi.org/https://doi.org/10.1016/j.engappai.2023.106000, 2023.

Loew, S. and Bottasso, C. L.: Lidar-assisted model predictive control of wind turbine fatigue via online rainflow counting considering stress history, Wind Energy Science, 7, 1605–1625, https://doi.org/10.5194/wes-7-1605-2022, 2022.

Matlab: Deep Learning Toolbox, https://www.mathworks.com/help/deeplearning/, last accessed 27 July 2024, 2023.

Mendez Reyes, H., Kanev, S., Doekemeijer, B., and van Wingerden, J.-W.: Validation of a lookup-table approach to modeling turbine fatigue loads in wind farms under active wake control, Wind Energy Science, 4, 549–561, https://doi.org/10.5194/wes-4-549-2019, 2019.

Natarajan, A.: Damage equivalent load synthesis and stochastic extrapolation for fatigue life validation, Wind Energy Science, 7, 1171–1181, https://doi.org/10.5194/wes-7-1171-2022, 2022.

Nocedal, J. and Wright, S. J.: Numerical Optimization, Springer, New York, NY, 2nd edn., 2006.

Noppe, N., Iliopoulos, A., Weijtjens, W., and Devriendt, C.: Full load estimation of an offshore wind turbine based on SCADA and accelerometer data, Journal of Physics: Conference Series, 753, 072 025, https://doi.org/10.1088/1742-6596/753/7/072025, 2016.

NREL Forum: https://forums.nrel.gov/t/openfast-linearization-of-nrel-5mw-onshore-turbine/2573, openFAST: Linearization of NREL 5MW Onshore Turbine, last access on 01.08.2023, 2023.

Olatunji, O. O., Adedeji, P. A., Madushele, N., and Jen, T.-C.: Overview of Digital Twin Technology in Wind Turbine Fault Diagnosis and Condition Monitoring, in: 2021 IEEE 12th International Conference on Mechanical and Intelligent Manufacturing Technologies (ICMIMT), pp. 201–207, https://doi.org/10.1109/ICMIMT52186.2021.9476186, 2021.

OpenFAST, 2024: https://github.com/OpenFAST/openfast/, openFAST, last access on 29.07.2024.

Pacheco, J., Pimenta, F., Guimarães, S., Castro, G., Álvaro Cunha, Matos, J. C., and Magalhães, F.: Experimental evaluation of fatigue in wind turbine blades with wake effects, Engineering Structures, 300, 117 140, https://doi.org/https://doi.org/10.1016/j.engstruct.2023.117140, 2024.

Schreiber, J., Bottasso, C. L., and Bertelè, M.: Field testing of a local wind inflow estimator and wake detector, Wind Energy Science, 5, 867–884, https://doi.org/10.5194/wes-5-867-2020, 2020a.

Schreiber, J., Bottasso, C. L., and Bertelè, M.: Field testing of a local wind inflow estimator and wake detector, Wind Energy Science, 5, 867–884, https://doi.org/10.5194/wes-5-867-2020, 2020b.

Schröder, L., Dimitrov, N. K., Verelst, D. R., and Sørensen, J. A.: Wind turbine site-specific load estimation using artificial neural networks calibrated by means of high-fidelity load simulations, Journal of Physics: Conference Series, 1037, 062 027, https://doi.org/10.1088/1742-6596/1037/6/062027, 2018.

Sepasgozar, S. M. E.: Differentiating Digital Twin from Digital Shadow: Elucidating a Paradigm Shift to Expedite a Smart, Sustainable Built Environment, Buildings, 11, https://doi.org/10.3390/buildings11040151, 2021.

Song, Z., Hackl, C. M., Anand, A., Thommessen, A., Petzschmann, J., Kamel, O., Braunbehrens, R., Kaifel, A., Roos, C., and Hauptmann, S.: Digital Twins for the Future Power System: An Overview and a Future Perspective, Sustainability, 15, 2023.

Surucu, O., Gadsden, S. A., and Yawney, J.: Condition Monitoring using Machine Learning: A Review of Theory, Applications, and Recent Advances, Expert Systems with Applications, 221, 119 738, https://doi.org/https://doi.org/10.1016/j.eswa.2023.119738, 2023.

The MathWorks, Inc.: MATLAB and Statistics Toolbox Release [2022b], Natick, MA, 2022.

TurbSim(2023): https://github.com/old-NWTC/TurbSim, turbSim, last access on 01.08.2023.

Vettori, S., Di Lorenzo, E., Peeters, B., and Chatzi, E.: A virtual sensing approach to operational modal analysis for wind turbine blades, 2020.

Wan, E. and Van Der Merwe, R.: The unscented Kalman filter for nonlinear estimation, pp. 153–158, https://doi.org/10.1109/ASSPCC.2000.882463, 2000.

Wu, P., Liu, Y., Ferrari, R. M., and van Wingerden, J.-W.: Floating offshore wind turbine fault diagnosis via regularized dynamic canonical correlation and fisher discriminant analysis, IET Renewable Power Generation, 15, 4006–4018, https://doi.org/https://doi.org/10.1049/rpg2.12319, 2021.

Ziegler, L., Smolka, U., Cosack, N., and Muskulus, M.: Brief communication: Structural monitoring for lifetime extension of offshore wind monopiles: can strain measurements at one level tell us everything?, Wind Energy Science, 2, 469–476, https://doi.org/10.5194/wes-2-469-2017, 2017.